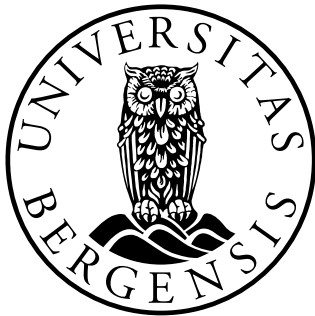# MASTER'S THESIS IN PHYSICAL OCEANOGRAPHY

**Decadal Variability and Trends of Atlantic Water and Adjacent Water Masses Along the Continental Slope West and North of Svalbard**

Stian Vikanes

Geophysical Institute - University of Bergen,
The University Centre in Svalbard (UNIS)

June 3, 2024

Date:     June 3, 2024
Title:    Decadal variability and trends of atlantic water and
          adjacent water masses along the continental slope
          west and north of Svalbard
Author:   Stian Vikanes

# Acknowledgements

# Abstract

In recent decades, the temperature of the West Spitsbergen Current north of Svalbard has risen substantially, with major implications for the Arctic Ocean and the Arctic sea ice cover. However, our understanding of long-term spatial and temporal variability remains limited. Using hydrography observations from the UNIS Hydrographic Database, combined with re-analysis sea ice and heat flux data, we investigate the decadal variability and trends along five climatological sections in the Svalbard Branch north of Svalbard, and analyze these observations in the context of air-ice-sea interactions. We show how the warm and saline Atlantic Water cools and freshens as it propagates along the continental slope north of Svalbard. The temperature in the upper 500 m changed on average with -0.30 °C per 100 km, corresponding to a vertical heat flux to the surface of up to 390 $\mathrm{W\,m^{-2}}$, however, with significant spatial variability between sections and temporal variability between decades. There was a reduced heat loss from the Svalbard Branch during 2000-2009, which we linked to increased surface meltwater and warmer adjacent water masses, due to a warmer and shallower Atlantic Water core, as well as changing wind patterns in this decade, pushing warm water onto the shelf. In 2010-2019, we observed a more saline surface layer with a subsequent weakened stratification, potentially caused by enhanced convective mixing, due to declining sea ice.

# Contents

# Chapter 1

# Introduction

More than a century ago, Nansen (1902) observed and described the Atlantic Water (AW), a warm and saline water mass carried by the West Spitsbergen Current (WSC), flowing towards the Arctic Ocean in the eastern Fram Strait (Fig. 1.1). Subsequent studies have underscored the importance of the AW, highlighting its role as a major source of heat, salt (e.g. Aagaard et al., 1987; Beszczynska-Möller et al., 2012) and nutrients (Torres-Valdés et al., 2013) for the Arctic Ocean. Consequently, the WSC plays a central role in the maintenance of the ice-free regions on the western and northern sides of Svalbard (Onarheim et al., 2014), supplying saline water for the formation of dense deep water (Swift & Aagaard, 1981; Aagaard et al., 1985) and driving significant primary production for the Arctic ecosystems (Oziel et al., 2020).

In the recent decades, the temperature of the WSC has increased substantially (e.g. Beszczynska-Möller et al., 2012; Pavlov et al., 2013; Tverberg et al., 2019; Polyakov et al., 2023), with great implications for the Arctic Ocean. Polyakov et al. (2017) described the so called "Atlantification" of the Eurasian Basin which is the term applied to the declination of sea ice with a subsequent reduction in stratification, increased vertical mixing and an altered primary production (Årthun et al., 2012). Surely, this has substantial effects for the entire Arctic system. North of Svalbard, there has been reported a sea ice area loss, during winter, of nearly 10% per decade since 1979 (Onarheim et al., 2014). The sea ice area loss concurs with a positive

trend in the AW temperature and a dramatic increase in the winter air temperature. Most of the sea ice loss in the area is attributed to the warming of the AW, along with favorable wind conditions that push the sea ice out of the region, favoring deep convection, deepening of the mixed layer depth and subsequent elevated heat fluxes (Onarheim et al., 2014; Carmack et al., 2015; Polyakov et al., 2017; Koenig et al., 2017b,a; Athanase et al., 2020; Fu & Myers, 2024).

The Svalbard Branch (SB) of the WSC (see Fig. 1.1) follows the 400 m isobath across the neck of the Yermak Plateau (YP), hugging the upper continental slope and continues eastward on the north side of Spitsbergen. The branch is considered to be strongly barotropic and therefore conserves its potential vorticity by following the isobaths (Perkin & Lewis, 1984; Aagaard et al., 1987; Koläs & Fer, 2018).

Several studies have explored the hydrography of the SB north of Svalbard (e.g. Boyd & D'Asaro, 1994; Cokelet et al., 2008; Våge et al., 2016; Koenig et al., 2017b; Koläs & Fer, 2018; Koenig et al., 2022). However, the majority of these studies have focused on observations limited to short time spans. They typically cover "snapshots" in time or seasonal variability. The data coverage north of Svalbard has in general been too sparse to be able to study the variability of the SB on longer timescales. Nonetheless, Saloranta & Haugan (2001) constructed a time series of available temperature and salinity data extending from 1910 to 1997 to study interannual variability north and north-west of Svalbard. In addition, there are some more studies looking into longer time scales on the western side of Svalbard (e.g. Pavlov et al., 2013; Skogseth et al., 2020; Muilwijk et al., 2018; Tverberg et al., 2019; Merchel & Walczowski, 2020). Consequently, our understanding of the temporal variability in the SB is limited to studies that focus on seasonal time scales and one longer, but sparse, time series by Saloranta & Haugan (2001), in addition to several upstream studies.

In this thesis, we will examine decadal variability and trends along the SB north of Svalbard. We will construct five cross-slope climatological sections (A-E; Fig. 1.1) for the July to November period, using historical hydrographic data from four consecutive decades between 1980 and 2020. Our goal is to describe and analyze changes in temperature and salinity. By
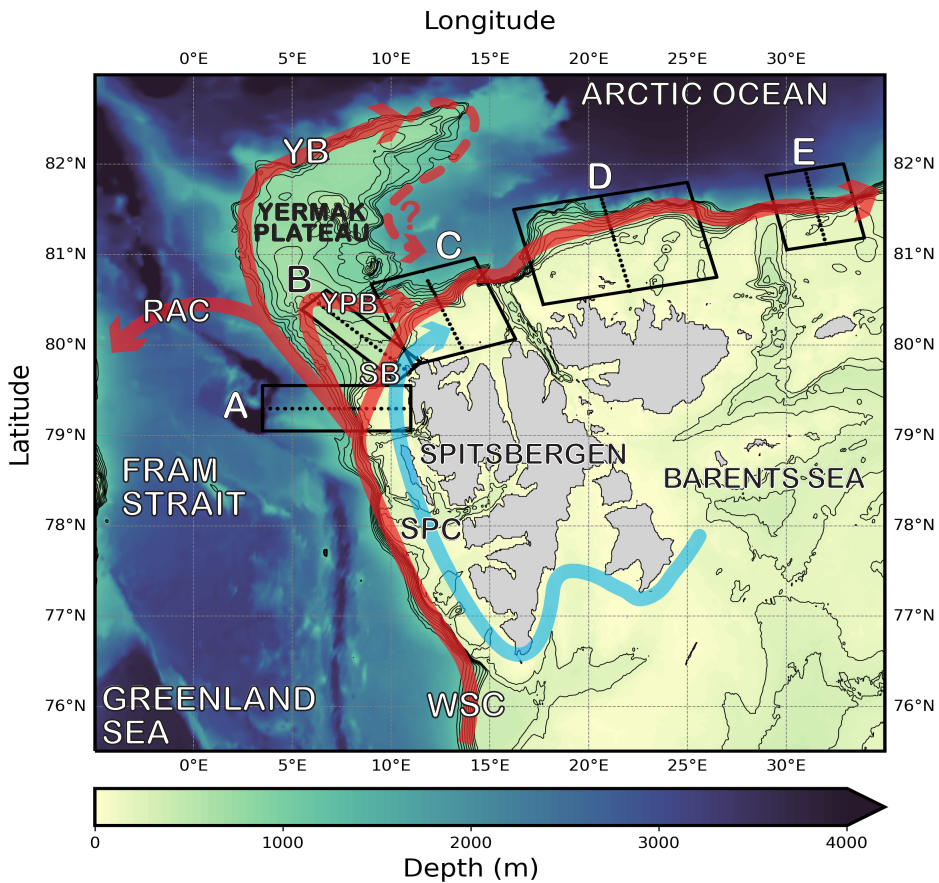
Figure 1.1: An overview of the study area. Black rectangles labeled A through E represent the areas where climatological sections are constructed and the black dots represent the bin centers. Red arrows depict the different pathways of the Atlantic Water in the West Spitsbergen Current (WSC) along the shelf-slope west and north of Svalbard. The Spitsbergen Polar Current (SPC) is depicted by the blue arrow. Other abbreviations yield: RAC = Return Atlantic Current, YB = Yermak Branch, YPB = Yermak Pass Branch and SB = Svalbard Branch. The ocean bathymetry is from the International Bathymetric Chart of the Arctic Ocean (IBCAO; Jakobsson et al., 2020) and is represented by the background colors. Isobaths from 200 m through 1200 m are shown with black contours.

comparing these findings with sea ice and heat flux data from re-analysis, we aim to enhance our understanding of air-ice-sea interactions in the region. Additionally, this study seeks to characterize the prevailing water masses, contributing to a deeper comprehension of the oceanographic dynamics in this area. The research questions we aim to answer through this study are:

1. What are the decadal changes in the water mass properties, such as temperature and salinity, in the SB from 1980 to 2020?

2. What are the spatial characteristics of the SB along the continental shelf north of Svalbard from 1980 to 2020?

3. How do atmospheric and oceanic factors influence the observed decadal trends and variability of the SB north of Svalbard?

The following chapter details the circulation and branching of the WSC in the regions west and north of Svalbard, explaining how the AW is modified as it interacts with local water masses, the atmosphere, and sea ice. Chapter 3 will present the data used in this study, and Chapter 4 will outline the methodology of the various analyses. In Chapter 5, we present the study's results, while Chapter 6 discusses these findings. Finally, Chapter 7 will summarize the study and answer the research questions, in addition to providing some suggestions for future work.

# Chapter 2

# Background

The northern branch of the Gulf Stream crosses the Greenland-Scotland Ridge carrying warm and saline waters from the North Atlantic into the Nordic Seas. Most of these water masses continue northwards along the west coast of Norway as the Norwegian Atlantic Current (Swift & Aagaard, 1981; Orvik & Niiler, 2002; Beszczynska-Möller et al., 2012). Beyond approximately 72°N the Norwegian Atlantic Current bifurcates into the two main streams of AW flowing into the Arctic Ocean. The first stream turns east through the Barents Sea Opening as the North Cape Current (Schauer et al., 2002; Smedsrud et al., 2013; Barton et al., 2018) while the second one follows the continental slope of West Spitsbergen, namely the WSC.

The WSC maintains a consistent average velocity of approximately 25 cm s$^{-1}$ along the 1000 m isobath, extending from Bear Island (74.5°N) to the Yermak Plateau (YP) (Boyd & D'Asaro, 1994). At the southern tip of the YP (79.5°N), the isobaths begin to diverge (Swift & Aagaard, 1981; Aagaard et al., 1987; Cokelet et al., 2008; Koläs & Fer, 2018) (See Fig. 1.1). The SB of the WSC follows the 400 m isobath across the neck of the YP and continues eastward along the north side of Spitsbergen (Perkin & Lewis, 1984; Aagaard et al., 1987; Koläs & Fer, 2018). The Yermak Branch (YB), on the other hand, keeps following the 1000 m isobath around the plateau (Schauer et al., 2004; Fer et al., 2023), and possibly rejoins the SB where the isobaths converge at approximately 13°E (see Fig. 1.1) (Perkin

& Lewis, 1984; Cokelet et al., 2008; Våge et al., 2016; Koläs & Fer, 2018). However, it does not follow the isobaths as closely, due to its baroclinic nature. The YB was reported to contain mesoscale eddies, shed at the point where the isobaths diverge (79.5°N) (Perkin & Lewis, 1984; Hattermann et al., 2016). Models and observations suggest that the YB further splits into three branches. One branch recirculates westward over the Fram Strait and joins the East Greenland Current, known as the Return Atlantic Current (Bourke et al., 1988; Teigen et al., 2011; Hofmann et al., 2021), the Yermak Pass Branch (YPB) which is shown to cross over the YP along the 700 m isobath (Gascard et al., 1995; Hattermann et al., 2016; Koenig et al., 2017b; Artana et al., 2022) and the rest of the YB that circulates around the plateau (See Fig. 1.1).

Flowing along-side the WSC is the Spitsbergen Polar Current (SPC; Fig. 1.1), which is the coastal current associated with the West Spitsbergen Polar Front along the west coast of Spitsbergen (Helland-Hansen & Nansen, 1909; Nilsen et al., 2016; Tverberg et al., 2019; Skogseth et al., 2020). As it travels northward, it accumulates heat and freshwater from the coast and the fjord systems along western Spitsbergen and brings it north of Svalbard, thus contributing to the heat and freshwater input into the Arctic Ocean (Nilsen et al., 2021).

As the AW follows the WSC along its intricate pathways, it is influenced by local water masses, a colder atmosphere, and sea ice, leading to the formation of new water masses. The region has a complex water mass terminology, making it challenging to distinguish between them and understand their origins. Swift & Aagaard (1981) established a water mass terminology that differentiates the various water masses and the processes influencing them. In the Arctic Ocean, surface water is cold and fresh due to atmospheric cooling and sea ice melt (Cokelet et al., 2008). This surface water is termed Arctic Surface Water (ASW) or Polar Water (PW), depending on its temperature. AW, ASW, and PW are considered the sources of other water masses in the Arctic, either through mixing or local modifications. Beneath the AW lies the Lower Arctic Intermediate Water (LAIW), formed by atmospheric cooling and the sinking of AW, retaining a high salt content. Above the AW, we may find the Upper Arctic Intermediate Water (UAIW), which is AW modified by cooling and sea ice melt, resulting in colder but fresher and

hence, lighter water. If the UAIW continues to cool and freshen at the same rate, it eventually becomes Polar Intermediate Water (PIW), which typically constitutes the Arctic halocline (Swift & Aagaard, 1981; Aagaard et al., 1985; Cokelet et al., 2008; Koläs & Fer, 2018). Water mass definitions that we use in this study are given in Sec. 4.1.

The AW interacts with its surroundings and undergoes modifications in temperature and salinity. Previous studies have observed downstream gradients of these properties, including a winter cruise in January-February 1989 (Boyd & D'Asaro, 1994), a fall cruise in October-November 2001 (Cokelet et al., 2008), 50-year average properties for summer (August-October) and winter (March-May) spanning 1949-1999 (Saloranta & Haugan, 2004), and a summer cruise in August 2015 (Koläs & Fer, 2018). The observed along-path freshening of the AW-layer (100-500 m) ranges from 0.010 to 0.015 $g\,kg^{-1}$ per 100 km, while the cooling rates are estimated to be 0.19-0.23 °C per 100 km in summer and 0.3-0.5 °C per 100 km in winter. The summer cooling rates (of the 100-500 m depth range) correspond to a horizontal and/or vertical heat flux between 300 and 350 $W\,m^{-2}$. If all the heat is assumed to be released to the atmosphere and sea ice directly above, the total vertical heat flux (0-500 m) was estimated by Cokelet et al. (2008) to be 520 $W\,m^{-2}$. However, this is likely an overestimation due to the influence of horizontal processes. In fact, Koläs & Fer (2018) demonstrated that the vertical eddy heat flux alone is insufficient to account for these cooling rates. Boyd & D'Asaro (1994) suggested that, since the AW is often separated from the surface by strong stratification, the heat loss to the surface can propagate horizontally over large distances along isopycnals that connect the AW with the surface. This process is not expected to be of significance in the summer, as the isopycnals are flat and do not outcrop to the surface (Koläs & Fer, 2018). Additionally, summer air temperatures are not expected to drive significant vertical heat loss to the atmosphere (Koläs & Fer, 2018). Still, horizontal isopycnal mixing between water masses can be substantial and constitute a significant cooling of the AW flowing northwards. Teigen et al. (2010) showed that horizontal heat fluxes related to barotropic instability, could account for up to one-third of the total heat loss and Teigen et al. (2011) showed that baroclinic instability could facilitate a heat flux from the AW core of up to 240 $W\,m^{-2}$.

Recent studies have linked the declining sea ice area north of Svalbard and the increasing AW temperature to increased heat flux to the atmosphere and subsequent deep convection (Koenig et al., 2017a,b; Athanase et al., 2020; Fu & Myers, 2024). The increase in deep convection frequency results in weaker stratification and a deepened mixed layer depth, making it easier for the AW to reach the surface, thus creating a positive feedback loop that maintains the ice-free region.

# Chapter 3

# Data

## 3.1 Hydrographic Data

### 3.1.1 UNIS Hydrographic Database

The data applied in this study are a subset of the UNIS Hydrographic Database (UNIS HD; Skogseth et al., 2019). The UNIS HD is a collection of available hydrographic data from UNIS student and research cruises around Svalbard (0-34°E and 75-83°N), supplemented with available historical data from the same area by other institutions. For details, see Skogseth et al. (2019, 2020). For this thesis we will be using data from 1980 to 2019, within the areas of the predefined sections (see Tab. 4.2).

### 3.1.2 Recent Data

More recent CTD data from the Norwegian Marine Data Centre (NMDC) and Forsvarets Forskningsinstitutt (FFI) covering 2019 to 2021 have been added to the database to gain a better temporal data coverage. The data have been cleaned for outliers by using UNIS HD data from north of Svalbard as a reference database to perform a simple statistical analysis. In the surface layer (0-100 m) the least saline water turned out to be on practical salinity of $33.07 \pm 1.46$, while in the intermediate layer (100-1000 m) the most saline water was practical salinity of $34.98 \pm 0.4$. We assume that the UNIS

HD provides a representative picture of the water masses north of Svalbard and that our simple analysis justifies disregarding measurements with practical salinity below 31.5 and above 35.4. We disregard temperatures below $-1.8°C$, while the maximum temperature that we accept in this thesis is $7°C$ and is based on a time series, from the UNIS HD, of average July to November maximum temperatures of the AW in the Fram Strait , where the maximum observed temperature was $6.8°C$.

Datasets harvested from NMDC are listed in Tab. 3.1 and are hydrographic data collected by the Nansen Legacy project. Raw unpublished Moving Vessel Profiler (MVP) and CTD data from FFI have been shared with us for use in this thesis (Tab. 3.1). The dataset consist of almost 1100 MVP casts where each of them includes both downcasts and upcasts, in addition to periods where the profiler lays in the surface. Considering that the downcasts are approximately vertical, while the upcasts are relatively skewed because of the ship speed, we have decided to only care about the downcasts in this work. Another aspect that is important to emphasize is that the MVP covers maximum the top 350 meters of the water column, giving a high number of measurements near the surface, in contrast to the deeper parts.

Table 3.1: Data harvested from the Norwegian Marine Data Center (NMDC) and the FFI. The table gives the name, time and source of the specific cruises.

| Cruise | Time | Source |
|---|---|---|
| Mooring service Cruise | 2019 Nov. | (Sundfjord, 2022) |
| Q3 | 2019 Aug. | (Reigstad, 2022) |
| JC2-1 | 2021 July | (Jones, 2022) |
| JC2-2 | 2020-2021 | (Fransson, 2022) |
| Q4 | 2019 Nov. | (Søreide, 2022) |
| FFI | 2019 Sep.-Oct. | - |
| | 2020 Oct. | - |
| | 2021 Sep. | - |

## 3.2   Sea Ice Data

Daily sea ice data from $0 - 38°E$ and $78 - 83°N$ from July to November, 1980 to 2020, has been retrieved using E.U. Copernicus Marine Service

Information; https://doi.org/10.48670/moi-00168. The Operational Sea Surface Temperature and Sea Ice Analysis is a reprocessed product of daily, gap-free sea ice concentration data at a 0.05° x 0.05° horizontal grid resolution, using satellite and in-situ data (Good et al., 2020).

## 3.3   Heat Flux Data

Daily total net vertical heat flux data from $0 - 38°$E and $78 - 83°$N from July to November, 1980 to 2020, was taken from the dataset from ERA5 (Hersbach et al., 2023). The data are the sum of the variables *Mean surface net long-wave radiation flux*, *Mean surface net short-wave radiation flux*, *Mean surface sensible heat flux* and *Mean surface latent heat flux*. ERA5 is a reanalysis of the global weather and climate for the past eight decades and provides hourly estimates of atmospheric, ocean-wave and land-surface quantities.

## 3.4   Bathymetry Data

Bathymetry data used in the figures and calculations of this thesis is sourced from the International Bathymetry Chart of the Arctic Ocean Version 4.0 (IBCAO; Jakobsson et al., 2020).

# Chapter 4

# Methods

For the rest of this study, temperature ($\Theta$ [°C]) refers to conservative temperature, salinity ($S_A$ [g kg$^{-1}$]) refers to absolute salinity, density ($\rho_{sw}$ [kg m$^{-3}$]) refers to the potential density anomaly relative to the surface and Brunt-Väisälä frequency ($N^2$ [$s^{-2}$]) refers to the vertical stability or stratification of the water column. These properties are calculated by following the International Thermodynamic Equations of Seawater (TEOS-10; McDougall & Barker, 2011).

## 4.1 Water Masses

As shown in Tab. 4.1, we use the AW and Arctic Intermediate Water definitions as they were originally defined by Swift & Aagaard (1981). This definition uses a warmer upper boundary for the AW and the Arctic Intermediate Water than what is traditionally used by e.g. Aagaard et al. (1985); Cokelet et al. (2008); Koläs & Fer (2018). To capture the full extension of the AW in the respective sections it is defined as water with $\Theta \geq 3°C$ and $S_A \geq 35.06$ g kg$^{-1}$. As for the AW, we also modify the upper boundary of the temperature range for LAIW and UAIW (Swift & Aagaard, 1981). PW and ASW are defined according to Cokelet et al. (2008); Koläs & Fer (2018).

Table 4.1: Water Mass Definitions, modified from Swift & Aagaard (1981). Arctic Surface Water (ASW) and Polar Water (PW) are taken from Cokelet et al. (2008).

| Abbr. | Name | Salinity, $g\,kg^{-1}$ | Temperature, °C |
|---|---|---|---|
| AW | Atlantic Water | $S_A \geq 35.06$ | $\Theta \geq 3$ |
| LAIW | Lower Arctic Intermediate Water | $S_A \geq 35.06$ | $3 > \Theta \geq -1$ |
| UAIW | Upper Arctic Intermediate Water | $35.06 > S_A \geq 34.87$ | $\Theta < 2$ |
| ASW | Arctic Surface Water | $S_A < 34.87$ $35.06 > S_A \geq 34.87$ | $\Theta > 0$ $\Theta < 2$ |
| PW | Polar Water | $S_A < 34.56$ | $\Theta < 0$ |
| PIW | Polar Intermediate Water | $34.87 > S_A \geq 34.56$ | $\Theta < 0$ |
| DW | Deep Water | $35.13 \geq S_A \geq 35.06$ | $\Theta < -1$ |

## 4.2 Climatological Sections

Climatological Sections A to E (Fig. 1.1), of temperature and salinity, were formed from five rectangular areas (Figs. 1.1 and 4.1 and Tab. 4.2), oriented perpendicular to the shelf break west and north of Svalbard. These sections were computed for the four decades from 1980 to 2020, using data from July to November. Assuming topographical steering of water following the SB (Aagaard et al., 1987), we computed grids of averaged temperature and salinity by weighted bin-averaging and interpolation at predefined grid points/bin centers (Tab. 4.2). **First step:** we identify the data points contained in the predefined section areas (Fig. 4.1) and within the desired time period. **Second step:** we check if the data points are positioned above the continental slope (green in Fig. 4.1) or the continental shelf (blue in Fig. 4.1), where the 200 m isobath is defined as the continental shelf break. Data points above the continental slope are categorized based on the bathymetric interval between neighboring bin centers in isobath-following bins. Specifically, data points within the depth interval $[ED(k) + \frac{1}{2}(ED(k+1) - ED(k)), ED(k) - \frac{1}{2}(ED(k) - ED(k-1))]$, where $ED[k]$ is the Echo Depth at the $k_{th}$ bin center (Fig. 4.1), are assigned to the $k_{th}$ bin center. For data points above the

continental shelf, each bin center has its own rectangular bin, where the length of the bins is given by the half distance to each of the neighboring bin centers (see Fig. 4.1). The width of the bins is given by *dlat* and *dlon* in Tab. 4.2 and corresponds to the perpendicular distance from the section line made of the bin centers (see Fig. 4.1).
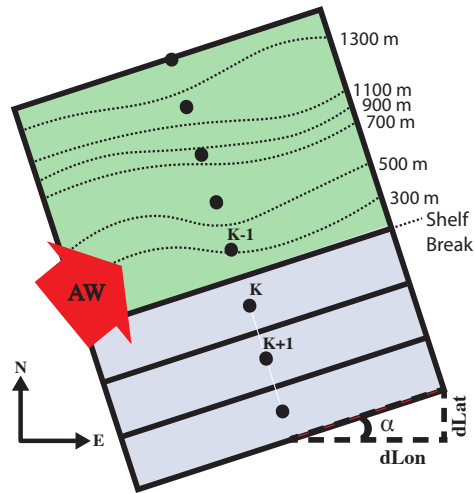


Figure 4.1: An illustration showing bin centers (black dots) on an idealized shelf (blue shading) and continental slope (green shading). Dashed lines on the continental slope represent isobaths from 300 m to 1300 m, and the shelf break indicate 200 m. The solid outer line represent the section area, while the black boxes on the shelf delineate the shelf bins. Delta-coordinates, *dlon* and *dlat*, together describe the width of the section area, while $\alpha$ describe the angle of the section relative to east.

**Third step:** once the data points are binned, they are given an averaging weight depending on their distance from the bin center. The points furthest away get a low weight, while the points close to the bin center get a high weight. Subsequently, a weighted average is calculated for each bin center. The (2D) grids consist of bin centers every 5 meter in the vertical and the procedure is repeated for every 5 m until 1000 m depth (or sea floor) to produce weighted bin-averaged grids of size 200 x $n$, where n is the number of bin centers horizontally (Tab. 4.2). **Fourth step:** when a bin average has been found for each grid point (200 x $n$), we use a Laplacian Spline Interpolation method with tension (Smith & Wessel, 1990; Koenig et al., 2022) to achieve a finer grid. For the interpolation method we use a 30 m x 30 km search radius without smoothing. The vertical resolution is set to 1 m while the horizontal resolution is set to 1 km, resulting in fine grids of size

Table 4.2: Detailed information about Sections A to E and their corresponding bin centers and areas. Coordinates of the first and last bin centers, including the distance between them, the number of bin centers (n) and the angle ($\alpha$) of the sections relative to East. The delta-coordinates (*dlat* and *dlon*) describe the widths of the areas corresponding to the sections.

|   | **Bin Centers** [$°N, °E$)] | **Dist** [km] | **n** | $\alpha$ [$°$] | **dlat** [$°N$] | **dlon** [$°E$] |
|---|---|---|---|---|---|---|
| A | $(79.30, 03.50) -$ $(79.30, 11.00)$ | 155 | 23 | 90.0 | 0.25 | 0.00 |
| B | $(80.50, 06.10) -$ $(79.70, 10.90)$ | 128 | 21 | 45.9 | 0.11 | 0.63 |
| C | $(80.82, 11.60) -$ $(79.92, 13.70)$ | 107 | 20 | 21.3 | 0.15 | 2.60 |
| D | $(81.65, 20.60) -$ $(80.60, 22.10)$ | 119 | 23 | 12.4 | 0.15 | 4.40 |
| E | $(81.94, 30.94) -$ $(81.12, 32.00)$ | 93 | 19 | 10.8 | 0.07 | 1.96 |

1000 x *dist*, where *dist* represents the horizontal distance (in km) between the first and last bin center in a section (Tab. 4.2). Climatological sections of density, are calculated from the already calculated salinity and temperature grids, and thereafter they are sorted vertically to avoid instability.

When computing the weighted bin-averaged temperature and salinity for each bin center in every 5-m depth layer, any bin represented by less than two years of data is ignored. Nilsen et al. (2021) conducted a similar analysis for the period 2006 to 2018 along a section corresponding to our Section B (Fig. 1.1), conditioning that each bin must include data from at least three years. However, despite the possibility of introducing biases, ensuring data coverage throughout the four decades in Sections A to E (Fig. 1.1), is prioritized in this study due to the lack of data in the northernmost sections.

Locations and other details about Sections A to E and the corresponding bin centers can be found in Tab. 4.2. The locations were carefully selected based on data availability, the results and locations of previous studies, and the assumption of a topographically guided SB flowing parallel to the shelf break. Sections A to C are largely covered in the literature (e.g. Saloranta

& Haugan, 2001; Cokelet et al., 2008; Koläs & Fer, 2018), Section D is previously described by e.g. Cokelet et al. (2008); Koenig et al. (2022), and Section E is covered by Cokelet et al. (2008); Våge et al. (2016); Pérez-Hernández et al. (2019) describing hydrography and velocity at 30°E.

After bin-averaging and interpolation, the data appeared noisy and needed filtering before plotting. We applied the Uniform Filter from the SciPy library (Virtanen et al., 2020), which smooths the data by linearly averaging values within a specified rectangular window. In this thesis, a window of 100 points vertically (100 m) and 20 points horizontally (20 km) was used.

The hydrographic sections in Secs. 5.1 and 5.5 and the stability sections (Sec. 5.6) are plotted from the filtered and interpolated (1000 x *dist*) grids. However, we use the weighted bin-averaged grids of size 200 x *n* for most calculations, including $\Theta - S_A$ diagrams in Sec. 5.1, cooling and freshening of the SB in Sec. 5.2, spatial variability in the SB (Sec. 5.3) and the calculated heat fluxes given in Sec. 5.4. The reason for this is to avoid introducing artificial values by the interpolation and extrapolation routines.

# 4.3   Annual Time Series

Annual time series of temperature and salinity for the AW are constructed using observational data from five polygons (Tab. 4.3) along the continental slope north of Svalbard. These polygons correspond geographically to Sections A-E (Fig. 1.1), but represent the areas of the sections that are containing the AW core. The calculations involve isolating the individual observations within Polygons A to E, for specific years, and vertically averaging them between 100 and 500 meters, to end up with one value that represents the 100-500 m layer each year. For the time series we use observational data between 1980 and 2021.

Table 4.3: Latitude and longitude coordinates delineating each Polygon A to E.

|     | A | B | C | D | E |
| --- | --- | --- | --- | --- | --- |
|     | 79.444 | 79.533 | 80.009 | 81.400 | 81.700 |
|     | 78.947 | 79.695 | 80.352 | 81.400 | 81.700 |
| **Lat** | 78.891 | 80.023 | 80.495 | 81.030 | 81.400 |
|     | 79.386 | 80.077 | 80.430 | 81.300 | 81.400 |
|     | 8.328 | 9.448 | 10.699 | 23.000 | 32.200 |
|     | 9.072 | 8.508 | 10.311 | 17.300 | 30.000 |
| **Lon** | 7.771 | 8.085 | 13.249 | 17.300 | 30.000 |
|     | 6.871 | 11.318 | 13.207 | 23.000 | 32.200 |

# 4.4 Changes En-Route the Svalbard Branch

## 4.4.1 Temperature and Salinity

The AW looses heat and salinity as it travels northeastward with the SB. We aim to track the maximum AW characteristics and the depth integrated changes along the SB of the WSC. To achieve this, we compute the mean temperature and salinity within three vertical ranges of the sections; 1) the surface layer from 0 to 100 m, 2) the AW layer from 100 to 500 m, and 3) the combined surface and AW layer from 0 to 500 m, extending horizontally from 35 kilometers inshore to 50 kilometers offshore relative to the shelf break (200-m isobath). Using this configuration ensures that we cover the AW core in all our sections. However, considering that Section B does not have 35 km of shelf, we needed to shift the area of estimation 20 km offshore to maintain the same cross-sectional area as for the other sections. By analyzing the maximum and average temperature and salinity values across all the sections, layers, and decades, we can ascertain the cooling and freshening rates en-route the SB through linear regression. Additionally, the depths at which maximum temperature and salinity occur are determined.

## 4.4.2 Heat Flux

Using the cooling rates en-route the SB, from Sec. 4.4.1, and assuming no horizontal heat fluxes, we can estimate the vertical heat flux going between the three different oceanic layers (with negative values representing upward heat fluxes). Following an approach modified from Boyd & D'Asaro (1994);

Cokelet et al. (2008); Koläs & Fer (2018), we have that the heat content, $\rho_{sw}c_{sw}\Theta$, of a sea water body changes in relation to the mean advection of heat and the eddy heat flux divergence

$$\rho_{sw}c_{sw}\left(\frac{\partial\overline{\Theta}}{\partial t} + \nabla\cdot(\overline{\mathbf{u}\Theta})\right) = -\rho_{sw}c_{sw}\nabla\cdot\overline{\mathbf{u}'\Theta'}. \qquad (4.1)$$

Here we have assumed incompressibility ($\nabla\cdot\mathbf{u} = 0$) and that molecular diffusion can be neglected in comparison to the eddy heat flux, $\overline{\mathbf{u}'\Theta'}$. $\mathbf{u} = \overline{\mathbf{u}} + \mathbf{u}'$ represents the velocity field. The overlines and primes indicate time averaged values and fluctuations from the averages, respectively. We integrate Eqn. (4.1) over a fixed volume, $V$, which represents the rectangular stream tube of the SB following the bottom topography between two cross-slope sections, and obtain

$$\rho_{sw}c_{sw}\int_{V}\left[\frac{\partial\overline{\Theta}}{\partial t} + \nabla\cdot(\overline{\mathbf{u}\Theta})\right]dV = -\rho_{sw}c_{sw}\int_{V}\nabla\cdot(\overline{\mathbf{u}'\Theta'})dV. \qquad (4.2)$$

Applying Gauss' Theorem on Eqn. (4.2) and assuming a steady state, yields

$$\rho_{sw}c_{sw}\int_{A(V)}\overline{\Theta}(\overline{\mathbf{u}}\cdot\mathbf{n})dA = -\rho_{sw}c_{sw}\int_{A(V)}(\overline{\mathbf{u}'\Theta'}\cdot\mathbf{n})dA, \qquad (4.3)$$

where $A(V)$ is the surface area of the volume $V$ and $\mathbf{n}$ represents the unit vector normal to $A(V)$. If we now assume heat loss only through the upper surface, $A_s$, a constant cross-sectional area, $A_c$, a constant along-isobath current velocity, $\overline{v}$, and perform the surface integrals of Eqn. (4.3), we get

$$\rho_{sw}c_{sw}A_c\overline{v}\frac{\partial\Theta}{\partial y}\Delta y = -(Q_a + Q_i)A_s, \qquad (4.4)$$

where $\Delta y$ is the en-route distance travelled by the current and $\frac{\partial\Theta}{\partial y}$ is the calculated downstream cooling rate over the distance $\Delta y$ along the SB.

Rearranging Eqn. (4.4), we get an expression for $Q_a + Q_i$, which are the vertical heat fluxes $[\text{W}\,\text{m}^{-2}]$ going to the atmosphere and melting of sea ice, respectively:

$$(Q_a + Q_i) = \rho_{sw} c_{sw} \bar{v} \frac{\partial \Theta}{\partial y} \Delta y \frac{A_c}{A_s}. \tag{4.5}$$

Above, $\rho_{sw} = 1025 \text{ kg}\,\text{m}^{-3}$ is the seawater density, $C_{sw} = 3850 \text{ J}\,\text{kg}^{-1}\,{}^\circ\text{C}^{-1}$ is the specific heat capacity of seawater, and $\bar{v} = 0.1 \text{ m}\,\text{s}^{-1}$ is the mean velocity of the SB, which is assumed to be constant and barotropic through all sections and decades (Saloranta & Haugan, 2004; Cokelet et al., 2008). A variety of different velocities have been used by previous authors, ranging from $0.05 \text{ m}\,\text{s}^{-1}$ to $0.2 \text{ m}\,\text{s}^{-1}$ (Aagaard et al., 1987). Using Eqn. (4.5) we can estimate the combined vertical heat flux from the ocean to the atmosphere and sea ice melt.

### 4.4.3  Temperature-Salinity Relationships

The ratio between the heat flux going to the atmosphere and the heat flux going to the sea ice melt can be derived from the slopes of a $\Theta - S_A$ diagram. Following Boyd & D'Asaro (1994) and Cokelet et al. (2008), who follow the conservation of heat and salt, we know that the temperature, $\Theta$, of a water mass with thickness $\Delta z$ will change in time by

$$\frac{d\Theta}{dt} = \frac{Q_a + Q_i}{\rho_{sw} c_{sw} \Delta z}, \tag{4.6}$$

if it is influenced both by heat loss to sea ice melt, $Q_i$, and heat loss to the atmosphere, $Q_a$. The salinity of the same water mass will change in time by

$$\frac{dS_A}{dt} = \frac{Q_i(S_A - S_i)}{L_i \rho_{sw} \Delta z}, \tag{4.7}$$

if it is influenced by sea ice melting. Here, $S_i = 5 \text{ g}\,\text{kg}^{-1}$ is the salinity of sea ice, and $L_i = 4281 \text{ J}\,\text{kg}^{-1}\,{}^\circ\text{C}^{-1}$ is the latent heat of fusion of pure ice.

The ratio of Eqns. (4.6) and (4.7) gives us an expression for $d\Theta/dS_A$, which we integrate from different initial points $(S_0, \Theta_0)$ to get an expression for $\Theta(S_A)$,

$$\Theta(S_A) = \Theta_0 + 79.2 \left(1 + \frac{Q_a}{Q_i}\right) \ln\left(\frac{S_A - S_i}{S_0 - S_i}\right), \qquad (4.8)$$

which, for a constant ratio of $Q_a/Q_i$, represents a slope in a $\Theta - S_A$ diagram. By comparing different slopes of $\Theta$ to the slopes of the actual measurements in our $\Theta - S_A$ diagram, we can give rough estimates of the ratio between $Q_a$ and $Q_i$.

## 4.5 Sea Ice and Heat Flux from Reanalysis

Sea ice data have been time averaged over four different decades from July to November and from 1980 to 2020, giving average values and standard deviations for every grid point that falls within the section Areas A to E (Tab. 4.2). These data have again been averaged to achieve one average sea ice concentration and one average standard deviation within the respective section areas and the four decades between 1980 and 2020. Same procedure has been done with the heat flux data from ERA5. The sea ice edge is defined as the 0.15 ice fraction (Parkinson & Cavalieri, 2008; Steele & Ermold, 2015).

## 4.6 Data Quality and Availability

Our temperature and salinity calculations output valuable information such as: the specific years (Fig. A.1) and months (Fig. A.2) represented in each section, including the standard deviations of temperature (Fig. A.3) and salinity (Fig. A.4) in every bin, as well as the number of observations (Fig. A.5) and the number of years (Fig. A.6) captured within individual bins. This information can be found in appendix A and are used for identifying and understanding potential biases, ensuring an objective assessment of the data. In the decade from 1980 to 1989, Sections A, B, and C exhibit a robust annual distribution, with data available for nearly all years (Fig. A.1). In contrast,

Sections D and E during this period are sparsely covered. The 1990-1999
decade shows gaps in yearly coverage and generally fewer measurements
compared to other decades (Fig. A.1). From 2000 to 2009, most years are
represented, though there is a notable concentration of data from 2005 to
2009 (Fig. A.1). The most recent decade (2010-2019) provides the strongest
coverage for the northernmost Sections C, D and E, but the data is heavily
skewed towards 2019 (Fig. A.1). Across most decades and sections, there is a
pronounced bias towards the summer months (July, August, and September),
with November being notably underrepresented (Fig. A.2). We see from
Tab. 4.4 how the two last decades are more representative for their respective
decades than the first two, with the median bin including 4 years instead
of 2 years. Additionally, the number of observations in the bins have also
increased (Tab. 4.4).

Table 4.4: The median number of observations / number of years represented in the non-
NaN bins. For Sections A to E and decades 1980-1989 to 2010-2019.

|   | 1980-1989 | 1990-1999 | 2000-2009 | 2010-2019 |
|---|---|---|---|---|
| **A** | 5 / 2 | 4 / 2 | 6 / 4 | 5 / 4 |
| **B** | 4 / 3 | 4 / 2 | 10 / 4 | 10 / 4 |
| **C** | 5 / 2 | 5 / 2 | 10 / 4 | 11 / 4 |
| **D** | 6 / 2 | 3 / 2 | 3 / 2 | 9 / 4 |
| **E** | 2 / 2 | 5 / 2 | 6 / 3 | 21 / 4 |

# Chapter 5

# Results

## 5.1 Hydrography and Water Masses

The decadal hydrographic cross-sections of Sections A to E (Fig. 1.1) over the period 1980 to 2019 have been computed from July to November data, and are shown in Figs. 5.1 to 5.5. The climatologies in this work cover the decades 1980-1989, 1990-1999, 2000-2009 and 2010-2019. From the figures it can be seen how the warm and saline AW propagates towards the north-east with the SB. We notice the general decrease in both temperature and salinity as the AW progress further into the Arctic Ocean.

Section A features a wedge-like AW domain with a thick end residing over the continental slope and a thin end reaching further offshore (Fig. 5.1). Since the turn of the millennium (Fig. 5.1g-l) AW has crossed the shelf break, but also the thin offshore end of the wedge has stretched even further offshore than previously and become thicker. In the last decade (Fig. 5.1j-l) the full extent of the AW offshore branch is not captured by our section and the AW has fully penetrated the surface layer above the shelf break. AW is in general dominating between 50 and 300 meter, but reaching as deep as 500 meter and up to the surface in the last decade. The water residing below the AW is the LAIW, which is AW transformed by cooling from the atmosphere. The surface layer is dominated by warm ASW (Fig. 5.1c,f,i

and l). From the $\Theta - S_A$ diagrams in the inset plots, we register that there are some PW observed in 1980-1989 and 1990-1999, linked to the cold and fresh pockets of water furthest offshore (Fig. 5.1a-b and d-e). Note that this is not captured in the water mass sections (Fig. 5.1c and f) due to the effect from smoothing of salinity and temperature.

In Section B (Fig. 5.2), which is located on top of the Yermak Plateau (Fig. 1.1), we find that the AW domain spread out more than in Section A (Fig. 5.1). The AW is in general extending deeper closest to the shelf/coast. A thin layer of UAIW is observed in the $\Theta - S_A$ diagram from 1980-1989 (Fig. 5.2c) furthest offshore between the ASW and LAIW.

Entering the Arctic Ocean, Section C (Fig. 5.3) contains an AW domain which is more closely confined to the shelf than in Sections A and B. In all decades, the AW $\Theta$-core is situated right above the shelf break. We notice that 2000-2009 is a warm and saline anomaly (Fig. 5.3g-i). A cold and fresh pocket of water can be observed in the surface layer furthest offshore of the two first decades (Fig. 5.3a-f). PW, PIW, and UAIW are related to this pocket of water in 1980-1989, according to the $\Theta - S_A$ diagram in the inset plot of Fig. 5.3c. The observed cold and fresh offshore surface water in 1980-1989 and 1990-1999 is no longer visible in 2000-2009 (Fig. 5.3g-i), but is again detectable to a smaller degree in 2010-2019 (Fig. 5.3j-l).

Moving to Section D (Fig. 5.4), the AW domain has moved off the shelf area. In 1980-1989 (Fig. 5.4a-c) there was hardly any AW left at this location, instead we observe UAIW and PIW in the shelf area and cold PW offshore. We find PW over the shelf in 1990-1999 (Fig. 5.4d-f). PIW and PW are not seen in Section D in 2000-2009 (Fig. 5.4g-i), but we observe a water mass close to UAIW over the shelf. In 2010-2019 (Fig. 5.4j-l) we find cold ASW furthest offshore, on the border to PW and PIW, including UAIW both offshore and over the shelf. The cold and fresh pocket of water furthest offshore and the anomalously warm and saline 2000-2009 are still visible in Section D. In addition, we observe colder and fresher water over the shelf compared to Sections A to C.

The warm anomaly in 2000-2009 continues to propagate eastward and is also clearly seen in Section E (Fig. 5.5g-i). Besides from the anomalous
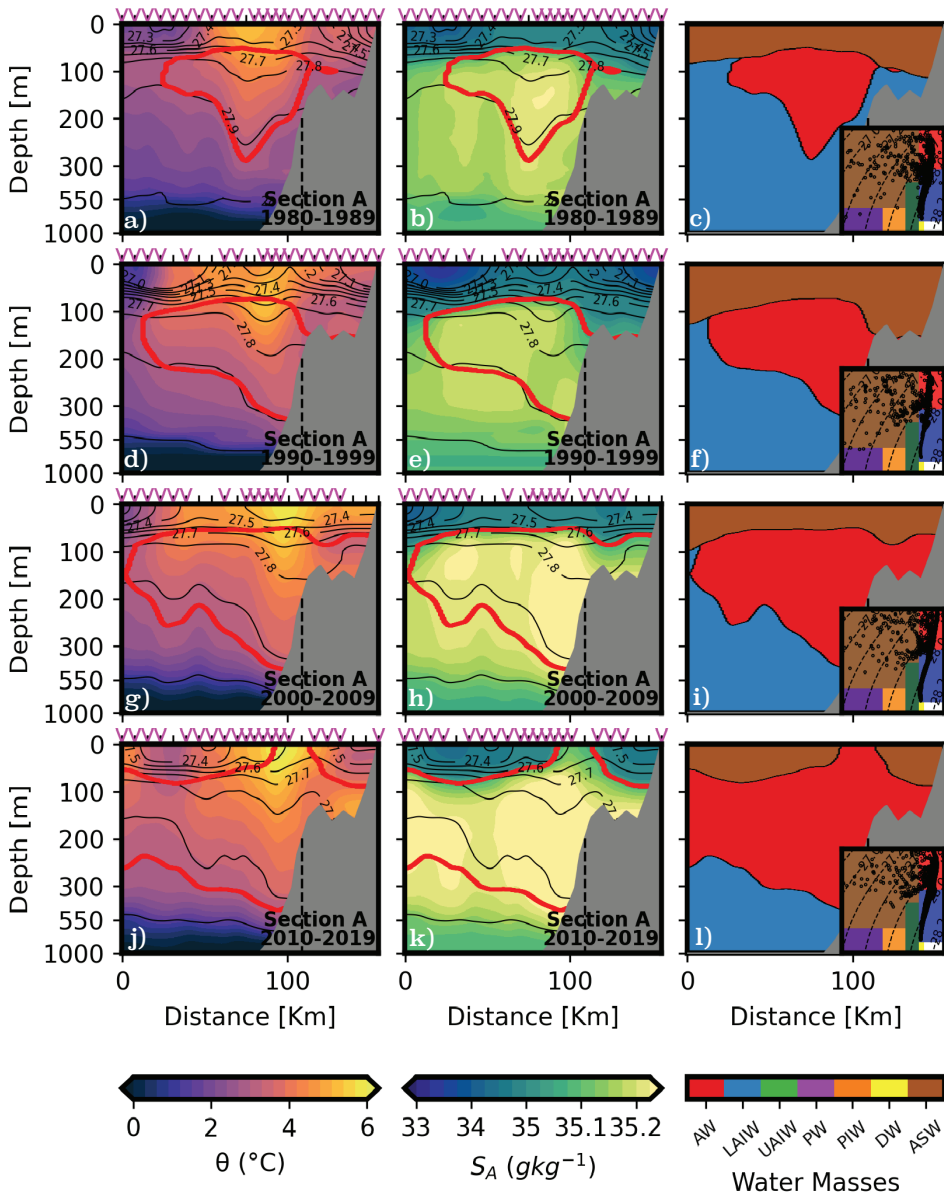
Figure 5.1: Decadal trends and variation of conservative temperature (a, d, g, and j) and absolute salinity (b, e, h, and k), accompanied by density contours, for Section A (Fig. 1.1) spanning 1980-2019. Each sub-panel represents a decade (1980-1989, 1990-1999, 2000-2009, and 2010-2019). The bottom bathymetry (from Jakobsson et al., 2020) is delineated in grey, with the shelf break denoted by a dashed black line, and the Atlantic Water highlighted by red contours. Dominant water masses are color coded and referenced by a $\Theta - S_A$ diagram (c, f, i and l), with definitions and abbreviations from Tab. 4.1. The horizontal distance is relative to the offshore bin center, and magenta triangles indicate where we have observations. The vertical resolution is linear down to 300 m and transitioning to logarithmic thereafter, while the salinity scale shifts resolution beyond 35 g kg$^{-1}$.
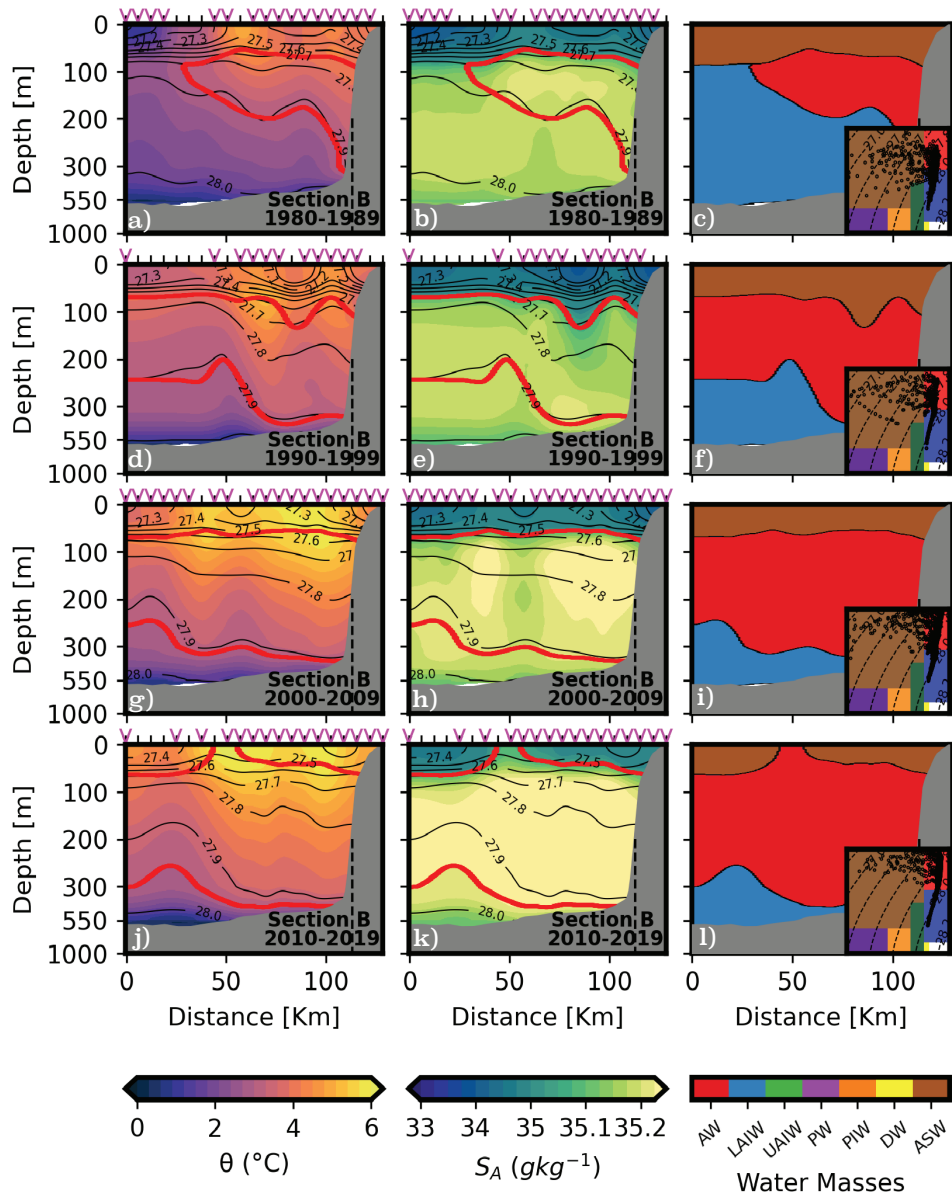
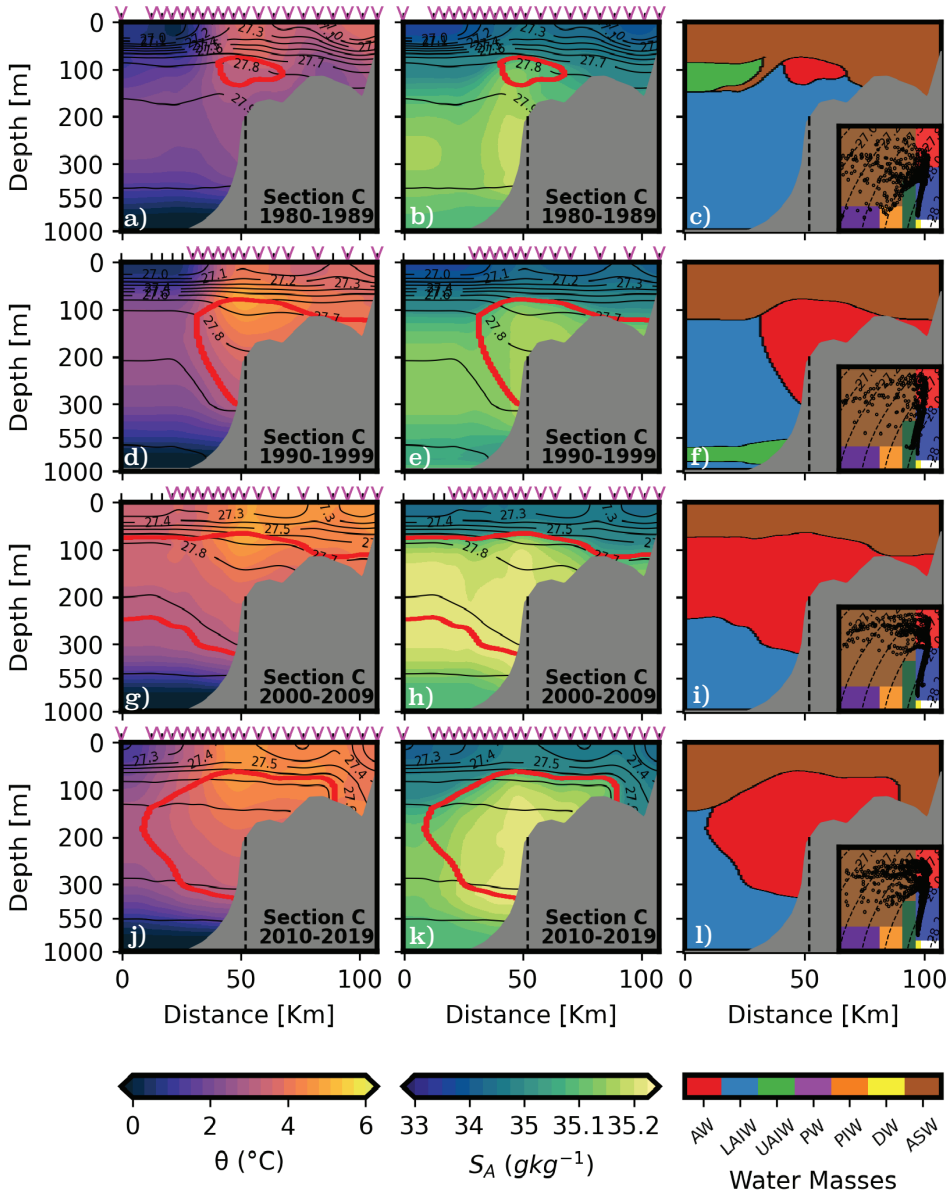Figure 5.2: Same as Fig. 5.1, but for Section B.

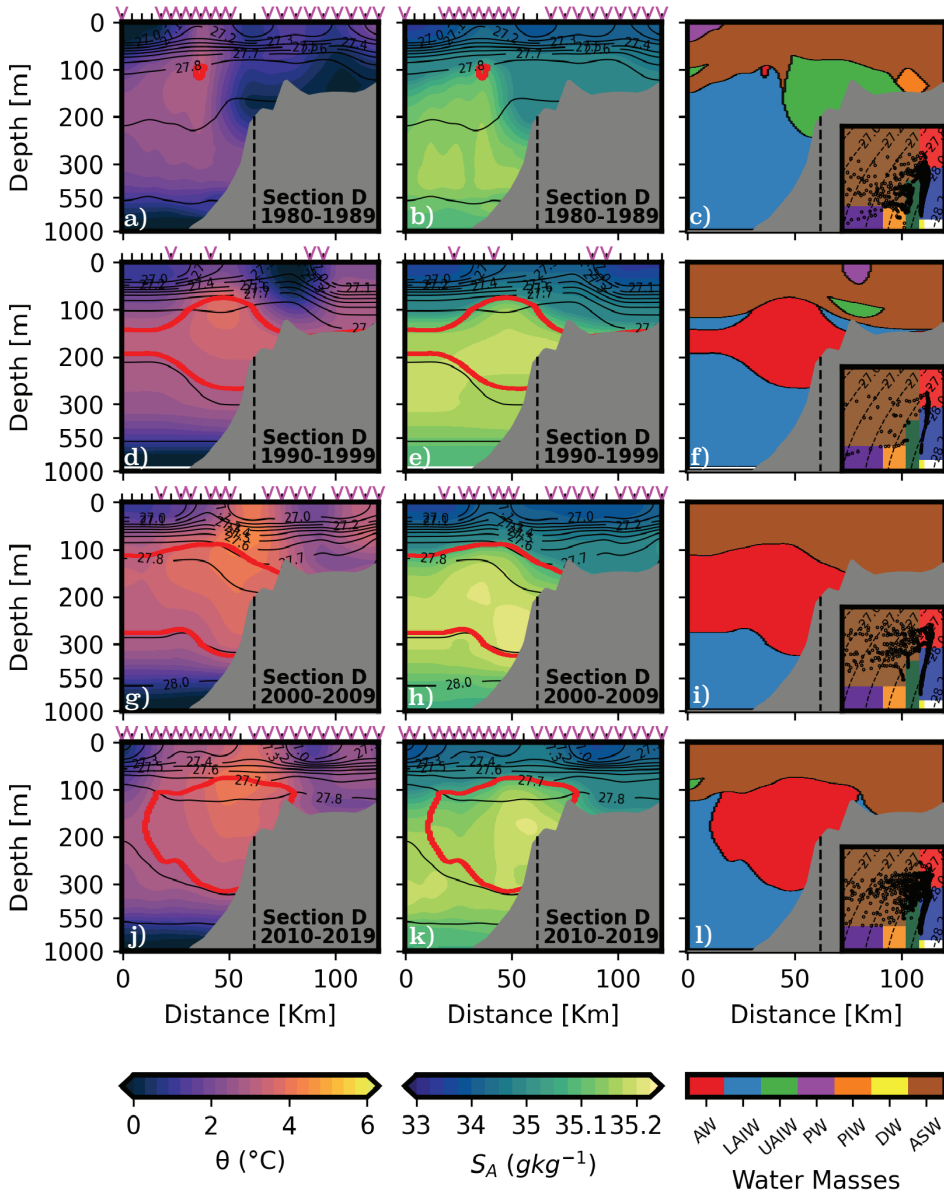Figure 5.3: Same as Fig. 5.1, but for Section C.

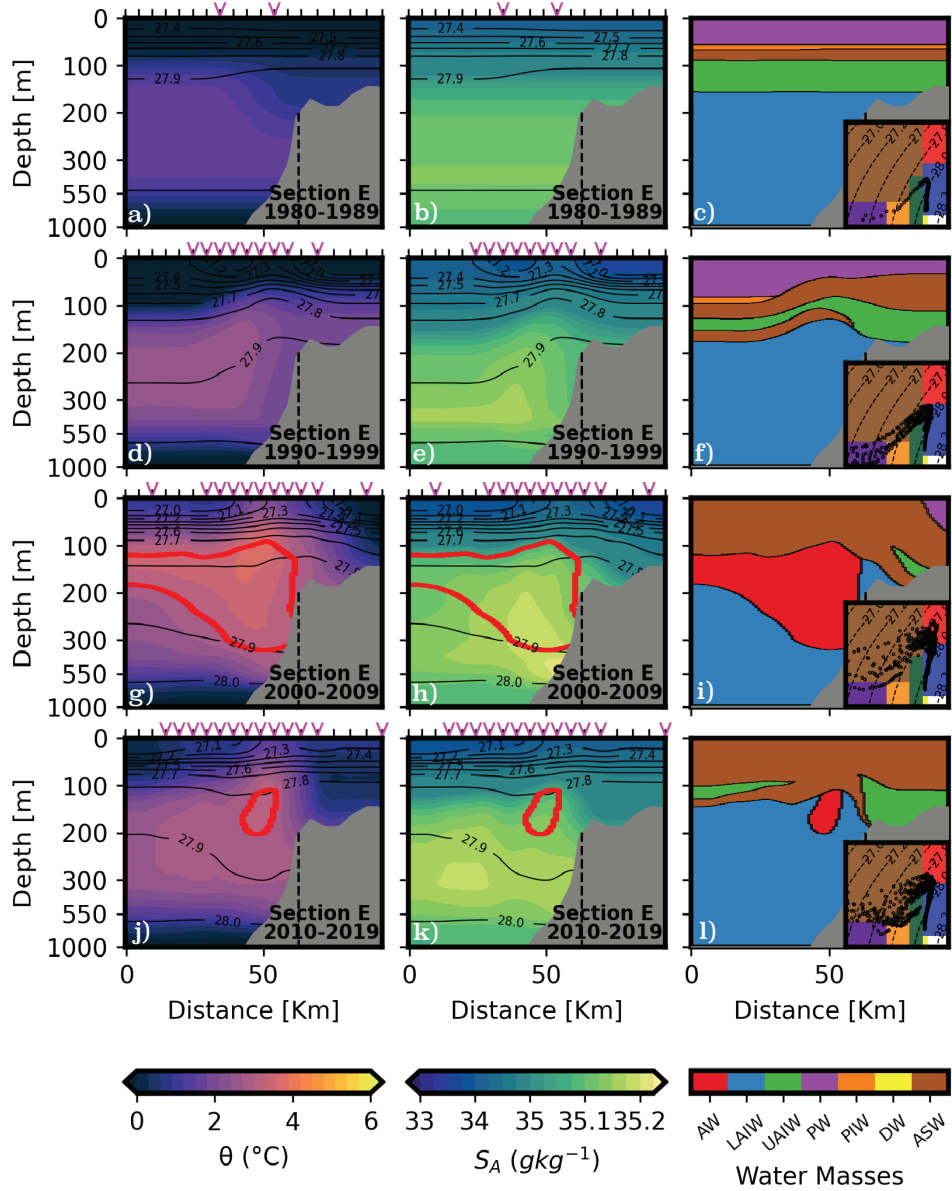Figure 5.4: Same as Fig. 5.1, but for Section D.

Figure 5.5: Same as Fig. 5.1, but for Section E.

decade, AW can hardly be seen in any of the decades. We notice that the AW in general has been replaced by UAIW and LAIW. PW and PIW are present in all years (inset $\Theta - S_A$ diagrams), however they are partly replaced by cold ASW in the two last decades (Fig. 5.5g-l). As in Section D (Fig. 5.4) we observe relatively cold and fresh water on both sides of the warm core.

Over time, the mean salinity and temperature have notably increased in all sections through 1980-1989, 1990-1999 and 2000-2009 (Figs. 5.1 to 5.5). The most pronounced change has been at Section E, where the mean temperature has increased from $1.6 \pm 0.5$ °C in 1980-1989 to $2.9 \pm 0.4$ °C in 2000-2009, and the maximum temperature has increased from 1.8 °C in 1980-1989 to 4.7 °C in 2000-2009 (see Tab. B.1). However, the mean temperatures in Sections C, D and E seem to be stagnating or decreasing from 2000-2009 to 2010-2019. On the contrary, the mean properties in Sections A and B seem to increase from 2000-2009 to 2010-2019 (Tab. B.1). Annual mean temperature and salinity of the AW-layer (100-500 m) are shown in Fig. 5.6. We notice that the mean salinity increases in all sections from 1980 to 2013, while there is a clear decreasing trend from 2013 to 2020 (Fig. 5.6b). The temperature also increases from 1980 to 2013, however with a continuous positive trend visible from 2013 to 2020 in Sections A to C, and a stagnating or decreasing temperature in Sections D and E (Fig. 5.6a). Linear regression gives a warming of the mean temperature in the 100 to 500 m layer in Section C by 0.34 °C per decade ($R^2 = 0.42$) and an increase in mean salinity of 0.018 $\mathrm{g\,kg}^{-1}$ per decade ($R^2 = 0.24$), prior to 2013. The same figure tells us that the mean salinity has decreased steadily in all sections from 2013 to 2020, with Section C decreasing by 0.015 $\mathrm{g\,kg}^{-1}$ per annum ($R^2 = 0.79$). The AW layer in Section A (corresponding to the Fram Strait) has a temperature increase of 0.30 °C per decade ($R^2 = 0.24$) from 1980 to 2020.

$\Theta - S_A$ diagrams give a good representation of the water masses and how they interact with the environment. In Figs. 5.7 and 5.8 we see that Sections A and C to E show similar characteristics in 2000-2009 and 2010-2019, with the warmest ASW above the AW core (red) and the shelf (blue), while the coldest ASW is located furthest offshore (green). However, we notice that generally all water masses are warmer in 2000-2009 than in 2010-2019. In addition we can see that the shelf water in Section E has become significantly
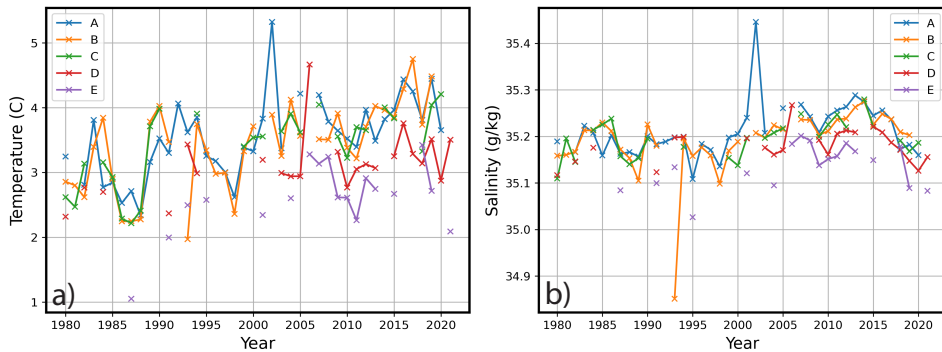
Figure 5.6: Annual (1980-2021) mean July-to-November temperature (a) and salinity (b) from Sections A to E (AW-layer; 100-500 m). Crosses represent the values, while solid lines connect values of consecutive years.

saltier in the last decade (Fig. 5.8d), compared to the previous one (Fig. 5.7d). All Sections have the signature heel from a high-heeled shoe, where the AW is loosing ten times more heat to the atmosphere than to sea ice melt ($Q_a/Q_i$ = 10). The LAIW is formed by this process.

In the $\Theta - S_A$ diagram of Section A from 2010 to 2019 (Fig. 5.8a), we observe a warm ASW over the whole surface layer of the section, with the warmest water laying over the AW core and shelf, while temperatures are increasing towards the surface ($Q_a/Q_i < 0$). Furthest offshore, the AW seems to cool and freshen according to the slope $Q_a/Q_i = 0$.

In the $\Theta - S_A$ diagram of Section C from 2010 to 2019 (Fig. 5.8b), we notice the warm ASW over the shelf and AW core region. The ASW in this region is as warm as the AW, but fresher. As we move offshore within the section, the ASW gets progressively colder, almost reaching PW at the most offshore bin center. In other words, $d\Theta/dS_A$ increases in the surface as we move offshore, with the offshore $d\Theta/dS_A$ indicating $Q_a/Q_i = 1$, and the on-shelf $d\Theta/dS_A$ not purely explained by heat loss to atmosphere and sea ice melt, but indicating that $Q_a/Q_i < 0$.

The $\Theta - S_A$ diagram for Section D from 2010 to 2019 (Fig. 5.8c) seems to be similar to the previous sections. The warmest surface water can be found above the AW core, with $d\Theta/dS_A$ increasing as we move offshore within the section. The $\Theta - S_A$ characteristics furthest offshore is steep enough
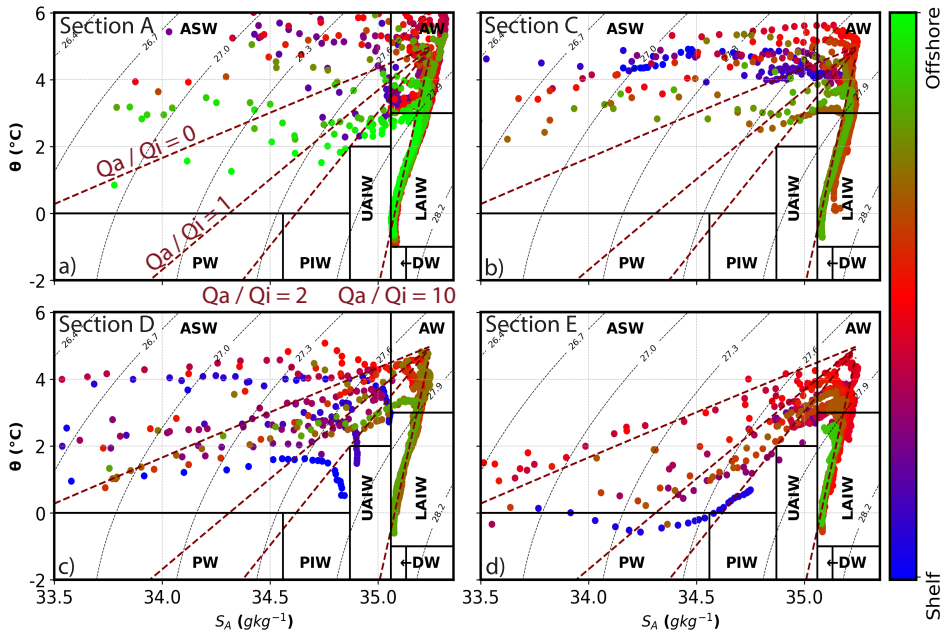
Figure 5.7: $\Theta - S_A$ diagrams from the decade 2000 to 2009 for Section A (a) and Sections C to E (b-d) (Fig. 1.1). Data points are color-coded based on their location in the section, with green indicating offshore and blue over the shelf. Red dashed lines depict mixing lines with constant ratios, $Q_a/Q_i$ (labelled in (a)). Black solid lines delineate different water masses which definitions are referenced in Tab. 4.1.

($Q_a/Q_i = 2$) to form UAIW and water on the border between ASW, PIW and PW, and the ASW follows a flat ($d\Theta/dS_A \approx 0$) slope towards the surface, along the border between ASW and PW. The ASW on the shelf exhibit a negative slope ($d\Theta/dS_A < 0$), implying diapycnal mixing between denser UAIW and warm/fresh ASW.

In the $\Theta - S_A$ diagram for Section E from 2010 to 2019 (Fig. 5.8d) a local temperature maximum at $\sim 1.0\ °C$ and $\sim 34.0\ \mathrm{gkg}^{-1}$ can be seen both offshore and over the shelf. Thereafter, the water is following a negative $d\Theta/dS_A$ towards a local temperature minimum as PW offshore and PIW over the shelf. Further progress of the $\Theta - S_A$ over the shelf is along a slope corresponding to $Q_a/Q_i = 2$ towards UAIW, while the offshore water approaches LAIW and AW following the $Q_a/Q_i = 2$ slope. The water located over the AW core seem to follow a slope similar to $0 < Q_a/Q_i < 1$.
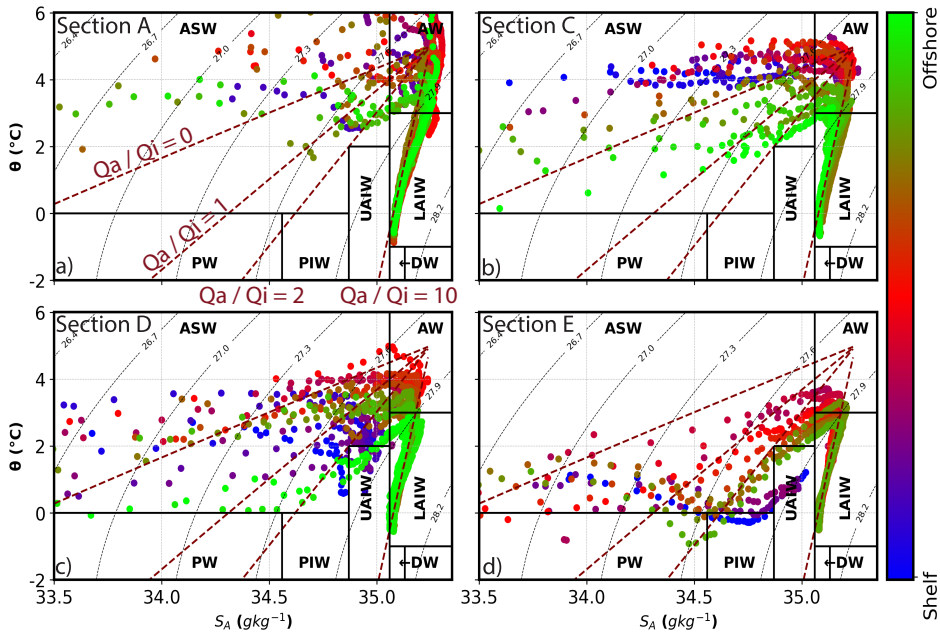
Figure 5.8: Same as Fig. 5.7, but for 2010-2019.

## 5.2    Cooling and Freshening of the Svalbard Branch

The temperature gradients in the AW layer (100-500 m) between Sections A and E range from -0.09 to -0.19 $°C$/100 km. The average values yield $-0.67°C$/100 km for the surface layer (0-100 m), $-0.16°C$/100 km in the AW layer, and $-0.30°C$/100 km in the combined surface and AW layer (0-500 m) (Tab. 5.1). The corresponding salinity gradients in the AW layer range from -0.004 to -0.020 $g\,kg^{-1}$/100 km, while the average values are -0.079 $g\,kg^{-1}$/100 km in the surface layer, -0.013 $g\,kg^{-1}$/100 km in the AW layer and -0.029 $g\,kg^{-1}$/100 km in the combined layer (Tab. 5.2). This means that the strongest heat and salinity loss is in the surface layer which is in contact with the atmosphere and sea ice.

There seem to be a systematic difference in heat loss between Sections A to C and Sections D to E (Tab. 5.1), where Sections A to C represents the first part of the AW pathway in the SB and Sections D to E is the last part. In the surface layer, the water seems to lose less heat between Sections A and C (average: -0.59 $°C$/100km) than between Sections D and E (average: -0.94 $°C$/100km). On the contrary, the AW layer seems to lose more heat

Table 5.1: Calculated temperature loss in °C per 100km between sections (A-E, A-C and D-E) for the surface layer (0-100 m), the AW layer (100-500 m), and the combined surface and AW layer (0-500 m) for each decade and the average over the decades.

|       | Layer [$m$] | 1980-1989 | 1990-1999 | 2000-2009 | 2010-2019 | Average |
|-------|-------------|-----------|-----------|-----------|-----------|---------|
|       | 0-100       | -0.76     | -0.75     | -0.53     | -0.65     | -0.67   |
| **A-E** | 100-500   | -0.18     | -0.18     | -0.09     | -0.19     | -0.16   |
|       | 0-500       | -0.32     | -0.36     | -0.21     | -0.31     | -0.30   |
|       | 0-100       | -1.17     | -0.21     | -0.32     | -0.65     | -0.59   |
| **A-C** | 100-500   | -0.46     | -0.31     | -0.26     | -0.36     | -0.35   |
|       | 0-500       | -0.71     | -0.31     | -0.30     | -0.46     | -0.45   |
|       | 0-100       | -1.23     | -0.99     | -0.49     | -1.04     | -0.94   |
| **D-E** | 100-500   | -0.36     | -0.29     | -0.13     | -0.22     | -0.25   |
|       | 0-500       | -0.50     | -0.44     | -0.21     | -0.43     | -0.40   |

between Sections A and C (average: -0.35 °C/100km) than between Sections D and E (average: -0.25 °C/100km). The salinity decreases more rapidly in both layers at the beginning of the AW pathway compared to the end. The surface layer loses on average 0.109 $\mathrm{g\,kg^{-1}}$/100 km in the first part and 0.012 $\mathrm{g\,kg^{-1}}$/100 km in the last part, while the AW-layer loses on average 0.024 $\mathrm{g\,kg^{-1}}$/100 km in the first part and 0.015 $\mathrm{g\,kg^{-1}}$/100 km in the last part.

Table 5.2: Same as Tab. 5.1, but for salinity loss [$\mathrm{g\,kg^{-1}}$ per 100km]

|       | Layer [$m$] | 1980-1989 | 1990-1999 | 2000-2009 | 2010-2019 | Average |
|-------|-------------|-----------|-----------|-----------|-----------|---------|
|       | 0-100       | -0.067    | -0.052    | -0.091    | -0.105    | -0.079  |
| **A-E** | 100-500   | -0.014    | -0.004    | -0.012    | -0.020    | -0.013  |
|       | 0-500       | -0.023    | -0.016    | -0.033    | -0.042    | -0.029  |
|       | 0-100       | -0.187    | -0.032    | -0.077    | -0.141    | -0.109  |
| **A-C** | 100-500   | -0.029    | -0.004    | -0.020    | -0.044    | -0.024  |
|       | 0-500       | -0.061    | +0.010    | -0.034    | -0.068    | -0.038  |
|       | 0-100       | -0.013    | +0.043    | +0.040    | -0.117    | -0.012  |
| **D-E** | 100-500   | -0.008    | -0.030    | -0.012    | -0.010    | -0.015  |
|       | 0-500       | +0.028    | +0.033    | +0.030    | -0.023    | +0.017  |

## 5.3   Spatial Variability

Spatial and decadal variability of temperature and salinity in the AW layer can be investigated from Fig. 5.9. We observe a general decrease in both mean and maximum properties as the AW travels from Section A to Section E (Fig. 1.1), however with significant variations. In the two first decades (Fig. 5.9a and b), the maximum temperature drops faster than the mean temperature, while in the last two decades (Fig. 5.9c and d) they decrease approximately at the same rate. All values in the figure can be found in Tab. B.1.

The maximum temperature is stagnant or barely increases between Section A and B in the two last decades (Fig. 5.9c-d), maintaining 6.6 °C in 2000-2009 and increases from 6.7 °C to 6.8 °C in 2010-2019. Mean temperatures are constant over the same distance (Fig. 5.9c-d). Moving from Section B to Section C, both temperature and salinity drop rapidly, being more rapid in 2010-2019, where the mean temperature drops from $3.7 \pm 0.5$ °C to $3.0 \pm 0.5$ °C and the mean salinity drops from $35.25 \pm 0.03$ g kg$^{-1}$ to $35.17 \pm 0.05$ g kg$^{-1}$. The rapid temperature and salinity decrease from Sections A/B to C is also reflected in Tabs. 5.1 and 5.2, where both properties decrease fastest in the first part (Sections A to C). From Section C to Section D, the mean temperature remains nearly constant, with a weak increase observed in the periods 1980-1989 and 2000-2009 (Fig. 5.9a,c). We notice how the differences in maximum temperature between Sections C and E are -2.6 °C and -2.8 °C in 1980-1989 and 1990-1999, and -0.9 °C and -1.6 °C in 2000-2009 and 2010-2019.

In Section A the maximum temperature remains constant at 25 m depth, except for the decade 1990-1999, where it dives down to 45 m, while the maximum salinity switches between 85 m and 100 m (Fig. 5.9). The temperature and salinity maximum in Section B has historically been located at 35-45 m and 95-100 m depth, respectively. However, in the last decade (2010-2019) the temperature maximum reaches all the way to the surface (Fig. 5.9). In Sections C, D and E we notice how the salinity maximums are significantly shallower in decade 2000-2009 (75 m, 165 m and 125 m, respectively), relative to the other decades. The depth of the temperature maximum in Section E changes significantly, with the temperature maximum
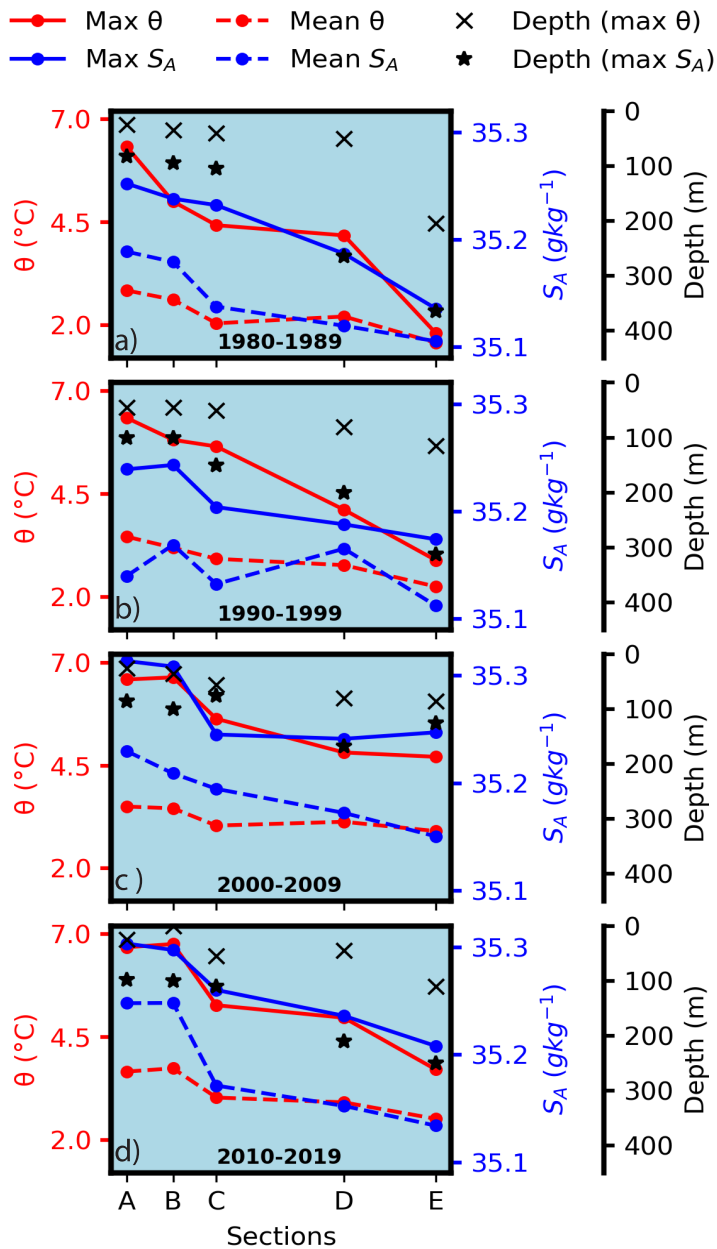
Figure 5.9: Spatial and decadal variations in temperature (red) and salinity (blue) across Sections A to E (Fig. 1.1) for the decades 1980-1989 (a), 1990-1999 (b), 2000-2009 (c), and 2010-2019 (d). Depths of maximum values are represented by black crosses for temperature and stars for salinity. Solid lines depict maximum values, while dashed lines represent mean values. Mean values are from the AW layer (100-500 m), while the maximum values are from water with $S_A \geq 35.06$.

rising from 205 m and 115 m in the the two first decades (Fig. 5.9a-b) to 85 m and 110 m in the two last decades (Fig. 5.9c-d).

## 5.4   Sea Ice and Heat Fluxes

The entire area of Section A is in nearly ice free conditions through the whole averaging period, which is evident from Tab. 5.3, with ice fractions ranging from 2% to 3%. The ice edge (15%) divides Sections B and C into an offshore part and an on-shelf part, with ice conditions offshore and open water over the shelf, however, in the last decade (Fig. 5.10d) the part with open water has increased. Similarly, according to decadal mean values in Tab. 5.3, Sections B and C are mostly located in ice covered areas from 1980 to 2009 (17-24%), while from 2010 to 2019 they are dominated by open water with mean ice fractions of 11%, however, with a large standard deviation. Sections D and E are located well within ice covered regions through all decades, however, with a rapid continuous sea ice decrease (Tab. 5.3) and the ice edge closing in from west and south (Fig. 5.10). In fact, the ice edge barely enters Section D in 2010-2019 (Fig. 5.10d). Between the two last decades, we notice a significantly higher sea ice loss than previously, where all sections from B to E lose an amount of sea ice corresponding to $\sim 35 - 40\%$ (Tab. 5.3).

The decadal mean net vertical heat flux from the ocean to the atmosphere in and around the respective sections north of Svalbard (Fig. 1.1), according to ERA5 reanalysis data, can be investigated from Tab. 5.4 and Fig. 5.11. We see a clear distinction in heat fluxes between the southernmost Section A and

Table 5.3: Decadal mean sea ice fraction in Sections A to E (Fig. 1.1), spanning 1980 to 2019.

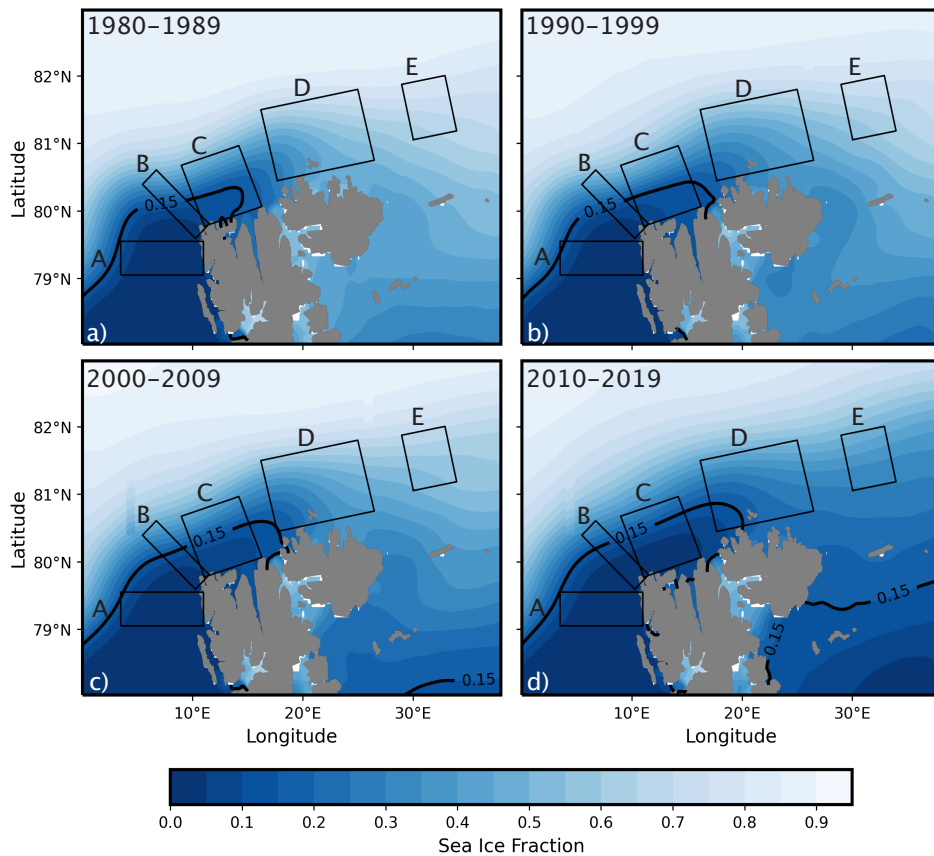|       | 1980-1989 | 1990-1999 | 2000-2009 | 2010-2019 |
|-------|-----------|-----------|-----------|-----------|
| **A** | $0.02 \pm 0.06$ | $0.03 \pm 0.07$ | $0.02 \pm 0.06$ | $0.02 \pm 0.06$ |
| **B** | $0.18 \pm 0.17$ | $0.19 \pm 0.20$ | $0.17 \pm 0.20$ | $0.11 \pm 0.15$ |
| **C** | $0.24 \pm 0.23$ | $0.23 \pm 0.25$ | $0.18 \pm 0.24$ | $0.11 \pm 0.17$ |
| **D** | $0.53 \pm 0.31$ | $0.44 \pm 0.35$ | $0.42 \pm 0.32$ | $0.28 \pm 0.31$ |
| **E** | $0.72 \pm 0.27$ | $0.66 \pm 0.30$ | $0.60 \pm 0.32$ | $0.38 \pm 0.35$ |

Figure 5.10: Decadal mean sea ice fraction north of Svalbard from 1980-1989 (a), 1990-1999 (b), 2000-2009 (c) and 2010-2019 (d) and in between July to November. The black contours denote the mean location of the ice edge (defined as 15% ice fraction) in the respective decades, while the black rectangles delineate the areas of Sections A to E (Fig. 1.1).

the northernmost Sections B-E, whereas in Section A we observe a relatively high heat flux (-98 to -82 $W m^{-2}$) compared to the northernmost sections (Tab. 5.4). This is also evident from Fig. 5.11 where we can see a clear maximum on the west side of Spitsbergen, with values on the order of -120 $W m^{-2}$. In the first three decades (Fig. 5.11a-c) there is a local maximum in heat flux located between Sections C and D.

In the last decade (Fig. 5.11d) the two maximums merge together and create a more gradual transition in heat flux from Sections A to E. This is illustrated with the -60 $W m^{-2}$ contour (Fig. 5.11) that is more or less constant to

Table 5.4: Decadal mean net vertical heat fluxes [$W\,m^{-2}$] in Sections A to E (Fig. 1.1), spanning 1980 to 2019. Negative means heat loss from the ocean to atmosphere. From ERA5 reanalysis data.

|   | 1980-1989 | 1990-1999 | 2000-2009 | 2010-2019 |
|---|---|---|---|---|
| A | -98 | -82 | -82 | -88 |
| B | -59 | -45 | -54 | -79 |
| C | -48 | -37 | -45 | -69 |
| D | -23 | -29 | -27 | -49 |
| E | -5 | -9 | -10 | -24 |

the west of Spitsbergen before it "shoots" through Sections B, C and D in 2010-2019. In addition, Tab. 5.4 clearly shows us how the difference between Section A and the northernmost sections has significantly dropped in 2010-2019 compared to previous decades. Furthermore, the heat flux maximum that is located south of Section A (Fig. 5.11) decreases steadily from -127 $W\,m^{-2}$ in 1980-1989 to -118, -113 and -110 $W\,m^{-2}$ in 1990-1999, 2000-2009 and 2010-2019, respectively.

In Tab. 5.5, we show the calculated vertical heat fluxes, in three different depth intervals, following Eqn. (4.5). The 40-year averaged vertical heat flux between Section A and Section E (Fig. 1.1) yield -265, -250 and -390 $W\,m^{-2}$, for the surface layer, the AW layer, and the combined surface and AW layer, respectively (Tab. 5.5). Looking into the decadal variations, Tab. 5.5 suggests that the two first decades in general have a larger negative heat flux than the two last decades. Furthermore, 2000-2009 seems to be a low heat flux anomaly, with -210, -140 and -270 $W\,m^{-2}$, for the respective layers.

Tab. 5.5 also shows the heat fluxes in different parts of the SB AW pathway (Fig. 1.1). We see a clear spatial difference between the two parts of the AW pathway. The surface layer has an elevated negative heat flux between Sections D and E (on average -370 $W\,m^{-2}$), compared to Sections A-C (on average -230 $W\,m^{-2}$). However, in the AW layer it seems to be a higher vertical heat flux, on average, in the first part of the AW pathway compared to the last part, -550 and -395 $W\,m^{-2}$, respectively.
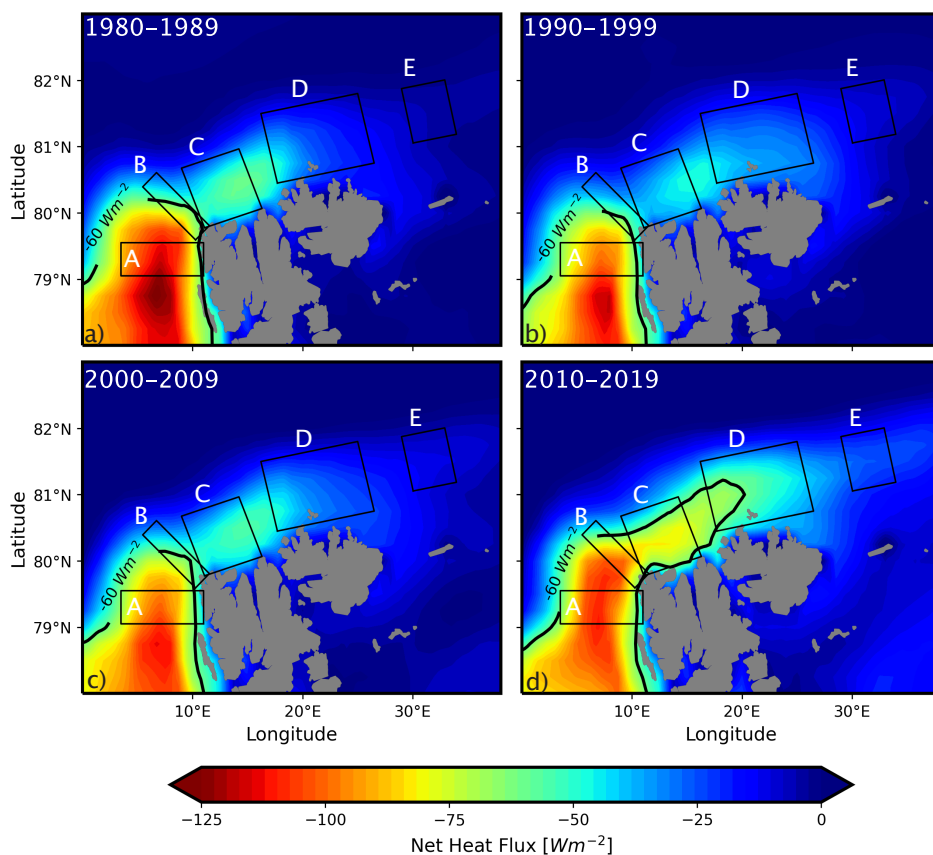
Figure 5.11: Decadal mean net vertical heat flux [$\mathrm{W\,m^{-2}}$] north of Svalbard averaged over June to November from 1980-1989 (a), 1990-1999 (b), 2000-2009 (c) and 2010-2019 (d). The black contours denote the mean location of the -60 $\mathrm{W\,m^{-2}}$ heat flux in the respective decades, while the black rectangles delineate the areas of Sections A to E (Fig. 1.1). Negative means heat loss from the ocean to atmosphere. From ERA5 reanalysis data.

Table 5.5: Calculated vertical heat fluxes [$\mathrm{W\,m^{-2}}$] between sections for the surface layer (0-100 m), the AW layer (100-500 m), and the combined surface and AW layer (0-500 m) for each decade, in addition to the average over the decades. Calculated by following Eqn. (4.5) and using values from Tab. 5.1.

|  | Layer | 1980-1989 | 1990-1999 | 2000-2009 | 2010-2019 | Average |
|---|---|---|---|---|---|---|
|  | 0-100 | -300 | -295 | -210 | -255 | -265 |
| **A-E** | 100-500 | -285 | -285 | -140 | -300 | -250 |
|  | 0-500 | -420 | -470 | -270 | -405 | -390 |
|  | 0-100 | -460 | -80 | -125 | -255 | -230 |
| **A-C** | 100-500 | -725 | -490 | -410 | -570 | -550 |
|  | 0-500 | -1400 | -610 | -590 | -910 | -880 |
|  | 0-100 | -485 | -390 | -195 | -410 | -370 |
| **D-E** | 100-500 | -570 | -460 | -205 | -350 | -395 |
|  | 0-500 | -985 | -870 | -415 | -850 | -780 |

## 5.5  Recent Observations (2020-2021)

Fig. 5.12 is showing the recent hydrographic characteristics for Sections C, D and E, averaged over 2020 and 2021, July to November. The recent characteristics seems to be colder and fresher than for previous decades (Figs. 5.3 to 5.5). Section C (Fig. 5.12a-c) has a strong horizontal temperature and salinity front at approximately 35 km (Fig. 5.12a-b), with AW and warm ASW occupying the shelf-side of the front, however only two bin centers capture the warm water, as indicated by the magenta triangles, while the rest of the shelf water is extrapolated from these two points. They can be identified as the warm ASW and AW in the $\Theta - S_A$ diagram in the inset plot of Fig. 5.12c. Offshore of the front we see LAIW transitioning directly into UAIW and cold ASW bordering PW and PIW. The AW detaches from the shelf in Section D (Fig. 5.12d-f), similar to previous decades (Fig. 5.4). Two AW cores are observed, where the smallest one is extending offshore out of the section (Fig. 5.12f). In Section E (Fig. 5.12g-i) there is no AW left. We see UAIW forming on top of the LAIW offshore of the shelf break, with cold ASW and PW residing in the surface (Fig. 5.12i). We notice that the surface water in Sections C and D is more saline compared to previous decades (Figs. 5.3 and 5.4), resulting in weakened surface stratification (Fig. 5.12b and e). By eye, the isopycnals appear to be further apart around the pycnocline.

The mean temperature in the AW layer of Sections C, D and E has decreased to $2.26 \pm 0.3$, $2.90 \pm 0.3$ and $1.96 \pm 0.1$ °C in 2020-2021 (not shown), from $3.0 \pm 0.5$, $2.9 \pm 0.5$ and $2.5 \pm 0.4$ °C in 2010-2019 (Tab. B.1). The mean salinity decreased to $35.09 \pm 0.03$, $35.08 \pm 0.02$ and $35.06 \pm 0.02$ g kg$^{-1}$ in 2020-2021 (not shown), from $35.17 \pm 0.05$, $35.15 \pm 0.05$ and $35.13 \pm 0.04$ g kg$^{-1}$ in 2010-2019 (Tab. B.1). Furthermore, the AW core has generally dived deeper than before, with the temperature core now located at 70 m, 45 m, and 165 m in Sections C, D, and E, respectively (not shown), compared to 55 m, 45 m, and 110 m in 2010-2019 (Tab. B.1). The salinity core is now at 125 m, 315 m, and 165 m (not shown), compared to 110 m, 210 m, and 250 m in 2010-2019 (Tab. B.1).
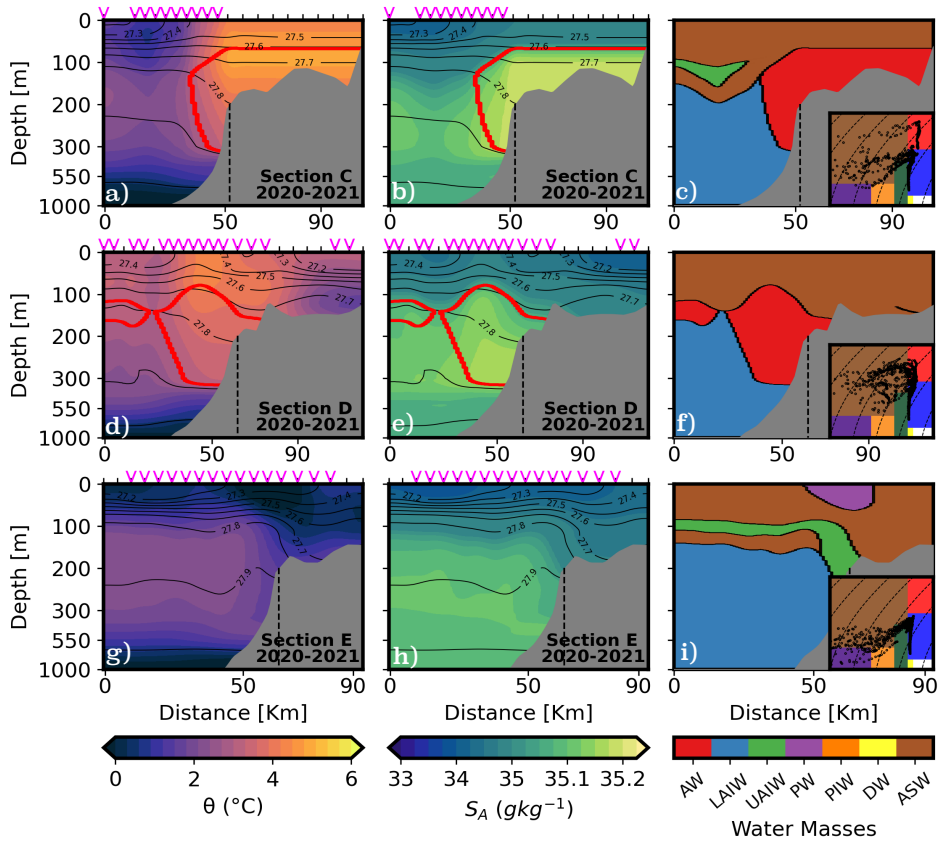
Figure 5.12: Recent characteristics of conservative temperature (a, d and g) and absolute salinity (b, e and h), accompanied by density contours, for Sections C (a-c), D (d-f) and E (g-i) (Fig. 1.1) spanning 2020 and 2021. The bottom bathymetry (from Jakobsson et al., 2020) is delineated in grey, with the shelf break denoted by a dashed black line, and the Atlantic Water highlighted by red contours. Dominant water masses are color coded and referenced by a $\Theta - S_A$ diagram (c, f and i), with definitions and abbreviations from Tab. 4.1. The horizontal distance is relative to the offshore bin center, and magenta triangles indicate where we have observations. The vertical resolution is linear down to 300 m and transitioning to logarithmic thereafter, while the salinity scale shifts resolution beyond 35 $\mathrm{g\,kg}^{-1}$.

## 5.6 Stability

The stability of the surface layer has decreased significantly in 2010-2019, especially for Sections A to C, as seen in Fig. 5.13. Section A (Fig. 5.13a-d) has historically been strongly stratified both offshore and over the shelf, with a slightly weaker stratification at approximately 70-100 km. In the last decade, the stratification has decreased offshore and almost vanished near the coast, compared to previous decades. We see the same situation at
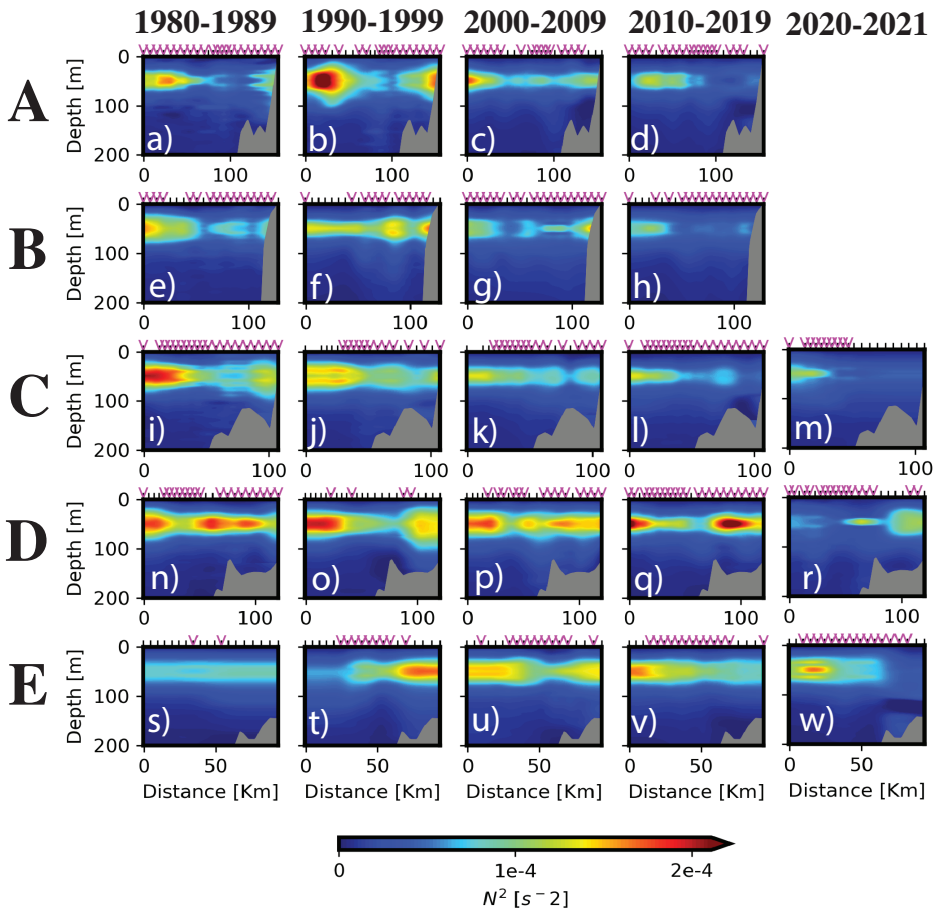


Figure 5.13: Decadal sections of the Brunt-Väisälä frequency, $N^2$ $[s^{-2}]$ for Sections A (a-d), B (e-h), C (i-l), D (n-q) and E (s-v) (Fig. 1.1) spanning 1980-2019. We also include the recent characteristics (2020-2021) from Sections C to E (m, r and w). The bottom bathymetry (from Jakobsson et al., 2020) is delineated in grey. The horizontal distance is relative to the offshore bin center, and magenta triangles indicate where we have observations. The vertical resolution is linear down to 200 m, only showing the surface layer.

Sections B and C (Fig. 5.13e-l), with the trend continuing into 2020-2021 (Fig. 5.13m). Sections D (Fig. 5.13n-q) seems to have gained an increased stratification both offshore and over the shelf in 2000-2009 and 2010-2019, followed by a decreases in 2020-2021 (Fig. 5.13r). The stratification in Section E (Fig. 5.13s-w) also decreases in 2020-2021 compared to previous decades, especially on the shelf side.

# Chapter 6

# Discussion

## 6.1 Hydrography

Section C for decade 2010-2019 contained warm and fresh ASW ($\Theta = 3.98$ °C, $S_A = 33.30$ g kg$^{-1}$) in the surface layer on the shelf-side of the section, while the offshore region contained a colder and fresher kind of ASW ($\Theta = -0.16$ °C, $S_A = 32.78$ g kg$^{-1}$) (Fig. 5.3j-l). The same pattern was also found by Koläs & Fer (2018) in August 2015. The warm and fresh surface layer above the shelf can be attributed to melt water from glaciers and sea ice, accumulated along the west coast of Spitsbergen by the SPC (Nilsen et al., 2021), and heated by short wave radiation early in the averaging period, when there was no sea ice. The colder ASW furthest offshore, where the sea ice coverage was larger (Fig. 5.10d), seems to have formed by ice melt alone, because $d\Theta/dS_A$ mainly follows the mixing line corresponding to $Q_a/Q_i = 0$ (Fig. 5.8b). Cokelet et al. (2008) called Section C a transition region, with sea ice conditions offshore and ice melting conditions onshore. This is similar to our finding, although the surface water in our section is up to 2 °C warmer, hence we get more sea ice melt offshore and radiative heating by the sun in the ice free regions over the shelf. The difference in surface water temperature can be attributed to our long averaging period from July to November, while their results were based on observations from October/November 2001. Sea ice fractions in Fig. 5.10d further supports

this hypothesis, illustrating how the ice edge on average divided Section C into an ice covered part offshore and an open sea part over the shelf (with high standard deviations due to the summer months (Tab. 5.3)). The decade 2000-2009 was an extraordinary warm and saline decade (average AW-layer: $3.0 \pm 0.4\ °C$ and $3.19 \pm 0.05\ \mathrm{g\,kg^{-1}}$), consequently the AW extend over the whole width of Section C (Fig. 5.3g-i) and the surface water is far from the freezing point temperature. However, there are no observations farthest offshore in 2000-2009 (Figs. 5.3g-i and 5.7b) to confirm the warm anomaly there. In 1980-1989 and 1990-1999, Section C (Fig. 5.3a-f) seems to have shown the same patterns in the surface water as 2010-2019, however with the cold offshore surface water extending both deeper and wider. The decrease in cold offshore surface water the past two decades, in Section C, is reflected by the dramatic decrease in sea ice fraction of 55%, from 1990-1999 to 2010-2019, shown in Tab. 5.3.

The surface water in Section D for decade 2010-2019 was cold and fresh ($\Theta = -0.06\ °C$, $S_A = 33.67\ \mathrm{g\,kg^{-1}}$) furthest offshore, while closest to the coast, over the shelf, we observed a warm water mass ($\Theta = 3.58\ °C$, $S_A = 34.27\ \mathrm{g\,kg^{-1}}$) that was blocked by a colder water mass further north on the shelf, towards the self break ($\Theta = 0.38\ °C$, $S_A = 33.02\ \mathrm{g\,kg^{-1}}$) and from underneath ($\Theta = 1.90\ °C$, $S_A = 34.96\ \mathrm{g\,kg^{-1}}$) (Fig. 5.4j-l). The same could be seen in 2000-2009 (Fig. 5.4g-i) and 1990-1999 (Fig. 5.4d-f). The shape of the $\Theta - S_A$ diagram in Section D for decade 2010-2019 (Fig. 5.8c) looks similar to the one found for Section 3 in Cokelet et al. (2008). Especially the offshore portion of the surface water, with 2.5 °C LAIW approaching PIW by cooling such that $d\Theta/dS_A$ corresponds to $Q_a/Q_i = 2$ and subsequently freshening along a flat $d\Theta/dS_A$ slope not explainable by $Q_a/Q_i$. Cokelet et al. (2008) explained the flat $d\Theta/dS_A$ as diapycnal mixing between fresh PW and saline PIW. On the shelf region of Section D, a negative $d\Theta/dS_A$ emerged. This implies that we at some point had diapycnal mixing between the relatively cold and saline UAIW, residing at the sea floor on top of the shelf, and a warmer and fresher ASW, which might have been transported there by the SPC (Nilsen et al., 2021). In 2000-2009 we did not have observations furthest offshore in Section D (Fig. 5.7c), but the shelf water seems to have gone through the same diapycnal mixing as in 2010-2019. In earlier decades (1980-1989 and 1990-1999) Section D had a colder shelf surface water (Fig. 5.4a-f). This was likely due to a larger sea ice fraction

(Fig. 5.10a-b), that insulated the water from the incoming solar radiation.

From the $\Theta - S_A$ diagram of Section E for decade 2010-2019 (Fig. 5.8d) we observed a local temperature maximum, at 1 °C and $\sim 34$ g kg$^{-1}$, close to the surface, both offshore and over the shelf. A negative $d\Theta/dS_A$, going towards a local temperature minimum of saline PW (offshore; $\Theta = -0.91$ °C, $S_A = 34.47$ g kg$^{-1}$) and PIW (over the shelf; $\Theta = -0.27$ °C, $S_A = 34.76$ g kg$^{-1}$), is implying diapycnal mixing between ASW-PW and ASW-PIW, respectively. The PIW over the shelf in Section E was formed from UAIW (residing on the sea floor, on the shelf, as seen in Fig. 5.5l) cooling along a $d\Theta/dS_A$ slope corresponding to $Q_a/Q_i \approx 2$, meaning that cooling by the atmosphere was twice as important as sea ice melt. The PW furthest offshore was also formed by cooling along a $d\Theta/dS_A$ slope corresponding to $Q_a/Q_i \approx 2$, however the source water in this case was LAIW (Fig. 5.5l and Fig. 5.8d). The shape of the $\theta - S_A$ diagram from Section E for decade 2010-2019 (Fig. 5.8d) was similar to what Cokelet et al. (2008) found in their corresponding Section 5, however their section did not include shelf water, consequently they could not verify UAIW as the main source water on the shelf. Furthermore, they defined UAIW and LAIW as 1 °C colder than in our study.

In a study by Muilwijk et al. (2018), an analysis of observed annual mean AW temperatures (50-700 m) in the Fram Strait (79°N) revealed a warming trend of 0.33 °C per decade from 1980 to 2012, similar to 0.30 °C per decade, as we found for Section A (100-500 m) in the period 1980-2020 (chapter 5 and Fig. 5.6a). Moreover, using the same depth interval (50-700 m) and time span (1980-2012) as Muilwijk et al. (2018), but for July to November instead of the whole year, we find an increase of 0.28 °C per decade in Section A in the period 1980-2020. However, our results indicated that the most significant temperature increase occurred prior to the decade 2000-2009, which was a notably warm period (see Figs. 5.1 to 5.5 and Fig. 5.6a). This warm period in 2000-2009 is supported by findings from Tverberg et al. (2019); Polyakov et al. (2023), both of which also confirmed that the positive temperature trend in the Fram Strait continued post-2009, albeit at a reduced rate. Conversely, in the Arctic Ocean, Sections C-E seems to have shown a stagnating temperature trend in the last decade (Fig. 5.6a). The dramatic salinity decrease (-0.015 g kg$^{-1}$ per annum) observed in all

sections after 2013 (Fig. 5.6b), was also seen by Polyakov et al. (2023);
Kolås et al. (2023) in the Fram Strait and Barents Sea. The reduced salinity
in the past decade is a signal that was transported from the source water in
the Atlantic Ocean, as shown by Polyakov et al. (2023).

In Sections C to E, the salinity maximum was located significantly closer to
the surface in 2000-2009 (75 m, 165 m, 125 m, respectively), compared to
the other decades (Fig. 5.9 and Tab. B.1). Since our observations were mainly
from the summer months, we believe that the temperature signature of the
AW core got hidden behind the strong surface water warming by radiation,
and therefore did not show as a shoaling in Sections C and D. However,
in Section E, also the temperature core of the AW was shallower in 2000-
2009 (85 m; Fig. 5.9 and Tab. B.1). We hypothesize that the temperature
signal of the AW in Section E was clearer due to the increased sea ice
(Tab. 5.3) that reflected the incoming solar radiation. Skogseth et al. (2020)
found the same AW shoaling in Isfjorden on the west coast of Spitsbergen.
They argued that there was a regime shift in 2006 (Cottier et al., 2007),
responsible for bringing warm and saline water closer to the surface and
onto the shelf (Nilsen et al., 2016). Polyakov et al. (2017) also showed a
substantial shoaling of the AW in the eastern Eurasian Basin of the Arctic
Ocean, especially in 2013-2014. There has been reported a salinification of
the surface water in recent years (Lind et al., 2018; Polyakov et al., 2017,
2020), which is also evident from our climatological sections (Figs. 5.1
to 5.5), contributing to the destabilizing of the water column as seen in
Fig. 5.13. A simple analysis like in Fig. 5.6, but for the surface layer, 0-100
m (see Fig. B.1), tells us that while the AW layer salinity decreased in the
last decade (Fig. 5.6b), the surface layer salinity continued its positive trend.

## 6.2   Cooling and Freshening of the Svalbard Branch

The average (1980-2019) July to November temperature and salinity gradi-
ents of the AW-layer along the SB from Section A to E (-0.16 °C/100km and
-0.013 g kg$^{-1}$ /100km) (Tab. 6.1), were comparable to previous reports from
the region north of Svalbard. Observations from October and November
2001 suggested -0.19 °C/100km and -0.013 g kg$^{-1}$ /100km (Cokelet et al.,
2008) from Sections A to E, while Saloranta & Haugan (2004) found -0.20

°C/100km and -0.010 $g\,kg^{-1}$ /100km as a 50-year August to October mean between 1949 and 1999, however, this was upstream of our Section A. More recently, Koläs & Fer (2018) reported -0.23 °C /100km and -0.015 $g\,kg^{-1}$ /100km with observations in August 2015 from an area corresponding to Sections A-C.

Similar cooling rates and freshening rates have been found both upstream of Section A (Saloranta & Haugan, 2004) and downstream of Section A (Cokelet et al., 2008). More than hundred years earlier Helland-Hansen & Nansen (1912) found a gradient of $-0.21°C$/100km on the west side of Spitsbergen between 75°N and 79°N, which implies that the cooling and freshening rate of the WSC has been the same over the last century, but also approximately the same from 74°N to 82°N (Cokelet et al., 2008). However, our findings suggest differently. The decadal variation in AW-layer temperature gradients from Sections A to E found in this work yielded $-0.18$ or $-0.19°C$/100km in all decades (Tab. 5.1) except for 2000-2009 that showed a significantly reduced gradient of -0.09 °C /100km, meaning that we do have temporal variability, which was also supported by the variable time series of the temperature gradient shown by Saloranta & Haugan (2004).

Looking into the spatial distribution of the cooling rates, we discovered significant differences between the first (Sections A-C) and last (Sections D-E) part of the AW-pathway in the SB. In the AW layer there seemed to be a greater temperature loss in the first part (ranging from -0.46 to -0.26 °C/100 km) (Tab. 5.1) than in the last part (ranging from -0.36 to -0.13 °C/100 km) (Tab. 5.1), which can be attributed to an AW core that travelled higher up in the water column between Sections A and C (see Fig. 5.9). Furthermore, a stronger surface stratification in Sections D and E (Fig. 5.13n-w) protected

Table 6.1: Average (1980-2019) temperature and salinity gradients and the vertical heat flux between Sections A and E in the surface layer, AW layer, and combined surface and AW layer.

| $z_1 - z_2$, [dbar] | $d\Theta/dy$, [°C/100 km] | $dS_A/dy$, [g/kg/100 km] | Q, [W m$^{-2}$] |
|---|---|---|---|
| 0-100 | -0.67 | -0.079 | -265 |
| 100-500 | -0.16 | -0.013 | - 250 |
| 0-500 | -0.30 | -0.029 | -390 |

the AW from the cold and ice covered surface. Conversely, in the surface layer it is evident that the temperature loss increased downstream (Tab. 5.1), which is expected since the atmosphere is colder and/or the surface has a higher ice concentration (Fig. 5.10) the more north and northeast we get. Nilsen et al. (2021) calculated the temperature gradients from Sections B to C and C to D (between the isobaths 110 and 550 m to only capture the slope water), based on a July-October climatology between 1993 and 2019. They found -0.30 $\pm$ 0.10 °C/100 km and -1.20 $\pm$ 0.10 °C/100 km, respectively. The cooling rate from Nilsen et al. (2021) between Sections B and C falls well within our calculations from Sections A to C. However, according to our estimations, Fig. 5.9 shows that the mean temperature barely decreased or increased between Sections C and D. A possible explanation for this is the influx of warm water from the rejoining YB (Fig. 1.1), which is believed to merge with the SB at approximately 13 °E (Perkin & Lewis, 1984). If this is the case, we would suggest that the two branches merge at 15 °E, earliest, based on our estimates.

Despite the AW layer losing less heat further north, it still lost a great amount (on average -395 $\mathrm{W\,m^{-2}}$) of heat (Tab. 5.5). Boyd & D'Asaro (1994) indicated that this heat loss can not be accounted for by diapycnal mixing alone, due to the strongly stratified surface water. The most important cooling mechanism in winter was suggested to be through mixing by eddies along isopycnals connecting the AW core and the surface or sea ice (Boyd & D'Asaro, 1994). Though, cooling by this process is not expected to be of great importance during July, August, and September because the relatively high air temperatures during these months do not drive significant heat loss (Koläs & Fer, 2018). However, isopycnal mixing between the AW-layer and the atmosphere seemed to be of some relevance in our constructed July to November climatologies, since the isopycnals that were going through the upper-bound of the AW domain outcropped in the surface some distance away, especially in the last two decades of Sections A and B (Figs. 5.1 and 5.2g-l). In addition, isopycnal mixing by eddies, between AW and adjacent water masses, might have accounted for a large portion of the heat loss (Teigen et al., 2010). In fact, Koenig et al. (2022) showed that lateral mixing must play an important role, using two mooring arrays north of Svalbard. Estimations using plausible eddy parameters from Crews et al. (2018), suggested that the contribution from these eddies could account for

up to half of the observed heat loss (Koläs & Fer, 2018).

The average vertical heat flux in the combined surface and AW layer (0-500 m) was calculated to -390 $\mathrm{W\,m^{-2}}$ (Tab. 6.1) from Sections A to E, and is the heat flux from the ocean to the atmosphere and sea ice melt directly above. The same results were -880 and -780 $\mathrm{W\,m^{-2}}$ for A-C and D-E, respectively (Tab. 5.5). Cokelet et al. (2008) calculated the corresponding value for Sections A to E to -520 $\mathrm{W\,m^{-2}}$, which they assumed to be an overestimation, due to horizontal mixing processes, as explained above. From looking at the $\Theta - S_A$ diagrams of Section E in 2010-2019 (Fig. 5.8), we observed that the surface water cooled with the atmosphere being twice as important as sea ice melt ($Q_a/Q_i = 2$), meaning that ($-780 \cdot \frac{2}{3} =$) -520 $\mathrm{W\,m^{-2}}$ went from the ocean to the atmosphere between Section D and E. Assuming that up to 50% of this heat flux was used to heat up adjacent water masses (Koläs & Fer, 2018), we are left with 210 $\mathrm{W\,m^{-2}}$ going directly to the atmosphere. However, this does not fit with heat fluxes in Sections D and E (2010-2019) from ERA5 in Tab. 5.4 and Fig. 5.11, which showed -49 and -24 $\mathrm{W\,m^{-2}}$, respectively, which is on the same order of magnitude as what was found by Moore et al. (2022), although they only included the turbulent heat fluxes.

## 6.3    Increased Deep Convection

As a result of a declining sea ice trend over recent decades, open ocean areas north of Svalbard have increased (Fig. 5.10), fostering an intensified air-ocean interaction. Studies by Athanase et al. (2020); Fu & Myers (2024) suggested that an intensified deep convective mixing in the region is sustaining ice-free areas by mixing AW into the surface layer. More deep convection contributes to an increased Mixed Layer Depth and a diminished stratification. Notably, in Sections A to C, we observed a substantially weakened stratification above the AW and shelf in 2010-2019 compared to the prior decades (Fig. 5.13a-l), which continued into 2020-2021, also in Sections D and E (Fig. 5.13m, r, w). This appears to have enhanced the convection of AW to the surface, as seen from the increased surface salinity in recent observations (Fig. 5.12). The weakened stratification in 2010-2019 and 2020-2021 is reflected by the notable reduction in sea ice fraction, as depicted in Fig. 5.10 and Tab. 5.3, and corresponds well with negative trends

in ice extent observed by Onarheim et al. (2014, 2018).

Increased vertical heat fluxes seen from ERA5 data in the latest decade (Fig. 5.11 and Tab. 5.4) fit well with a weakened stratification (Fig. 5.13), the AW being closer to the surface (Fig. 5.9), and a subsequent increased deep convection. We saw this especially in the northernmost Sections D and E where the heat fluxes to the atmosphere have increased by 55% and 59% (Tab. 5.4), respectively, in 2010-2019 compared to 2000-2009 (also shown, but not discussed by Moore et al. (2022)). Our calculated vertical heat fluxes (Tab. 5.5) support an increased heat loss (in the surface layer) between Sections D and E in 2010-1019 compared to 2000-2009. Moreover, according to our calculations, the SB seemed to lose significantly less heat in all sections in 2000-2009 compared to the other decades in our study (Tab. 5.5), which gives a good explanation for the anomalously warm decade. A reasonable question to ask is: why was the vertical heat fluxes (Tab. 5.5) significantly lower during 2000-2009 compared to 2010-2019? It has been shown that sea ice loss west and north of Svalbard accelerated during the decade 2000-2009, with a minimum extent in 2006/2007 (Stroeve et al., 2012; Muckenhuber et al., 2016; Polyakov et al., 2023). These observations coincided with the anomalously warm AW layer that flowed closer to the surface in the same decade (Fig. 5.9c). We hypothesize that this extreme sea ice melting created an insulating layer of fresh water that was advected northwards, hence the increased stratification in Section D 2000-2009 (Fig. 5.13p) and less temperature loss in the AW layer between Sections C and E (Fig. 5.9c). Additionally, Cottier et al. (2007); Nilsen et al. (2016) showed that a changed wind pattern in the same decade was responsible for pushing AW onto the shelf areas west of Svalbard, resulting in warmer water masses on the shelf. Warmer water masses on the shelf, but also offshore of the AW core, were observed in (Figs. 5.1 to 5.5), in 2000-2009. Consequently, due to melt water in the surface and warmer ambient water, the AW lost less heat both vertically and horizontally in 2000-2009. The decade 2010-2019, on the other hand, had already a reduced sea ice coverage (Fig. 5.10), exposing more ocean surface and enhancing convective mixing, as indicated by Athanase et al. (2020); Fu & Myers (2024). The weakly stratified conditions observed in 2010-2019 (Sections A-C) and 2020-2021 (Sections C-E) (Fig. 5.13) are consistent with this hypothesis.

## 6.4    A Critical Reflection

The level of confidence in our climatological sections varies significantly. The sections for the first two decades (1980-1989 and 1990-1999) are poorly represented, with only two years contributing to the median bin center (Tab. 4.4 and Figs. A.5 and A.6). This is despite Sections A-C showing a good yearly distribution in Fig. A.1 for 1980-1989. If we applied the same criteria as Nilsen et al. (2021), who required a minimum of three years represented in a bin center, we would barely be able to create any of the sections (A-E) for the first two decades. Furthermore, Fig. A.2 shows us that mostly July-September are represented in the first two decades (in addition to Sections A-C in 2000-2009), making the sections in these decades pure summer sections. The summer biased data coverage could make the surface layer in the sections appear warmer than they are in reality, due to the increased solar radiation. The same yields for the SPC, which was shown to be warmest in August/September (Nilsen et al., 2021). However, the AW-layer experiences its seasonal maximum in October/November (Nilsen et al., 2021; Koenig et al., 2022).

In 2000-2009, the bin centers of all sections exhibit a better yearly distribution compared to earlier decades, as seen in Tab. 4.4 and Figs. A.5 and A.6. However, there is a noticeable bias towards the end of the decade, a period known to contain the warmest years, as reported by Beszczynska-Möller et al. (2012); Skogseth et al. (2020); Polyakov et al. (2023). Therefore, we suspect that the average temperatures in this decade are warmer than the true average.

The northernmost sections (C-E) in the last decade (2010-2019) are strongly biased towards 2019 (Fig. A.1). This overrepresentation of 2019 in Sections C-E can be attributed to recent data from FFI, which are only represented in the upper 300 m, as seen in Fig. A.5. The climatological sections constructed in this study are referred to as July to November sections. However, this designation is somewhat misleading, as November is almost not represented, except for in the most recent decade (Fig. A.2). The Sections prior to 2010-2019 should, at most, be referred to as July to October sections.

We observe large standard deviations of temperature (up to 3.0 °C, Fig. A.3)

and salinity (more than $0.3\ \mathrm{g\,kg^{-1}}$, Fig. A.4) in the surface layer, reflecting seasonal variability due to the long time span of our measurements (July to November).

# Chapter 7

# Conclusions and Future Work

## 7.1 Concluding Remarks

The Arctic Ocean has experienced an increased global attention due to its sensitivity to climate change (IPCC, 2022). The challenging and remote conditions north of Svalbard makes data collection both costly and difficult, resulting in a sparsity of observational data in this region. Throughout this study, we have provided valuable insights into the hydrography north of Svalbard. Specifically, we have constructed five climatological Sections (Figs. 5.1 to 5.5), labelled A to E (Fig. 1.1), spanning from July to November across four consecutive decades between 1980 and 2020. This has allowed us to investigate spatial and temporal variability in the SB of the WSC. We have computed temperature and salinity gradients en-route the SB and compared the observed changes to sea ice conditions and vertical heat fluxes in the region.

The first research question we ask in Chapter 1 concerns decadal changes in water mass properties, such as temperature and salinity, in the SB from 1980 to 2020. The cooling rate of Section A in the Fram strait from 1980 to 2020, July to November, was found to be 0.30 °C per decade, similar to that (0.33 °C per decade) found by Muilwijk et al. (2018) from 1980 to 2012. However, our findings suggested that the most significant temperature

rise of the AW occurred prior to the warm decade 2000-2009, also seen by e.g. Tverberg et al. (2019); Polyakov et al. (2023). Post 2000-2009, the AW in the Fram Strait and over the Yermak Plateau (Sections A and B) continued to rise, while the sections (C-E) north of Svalbard showed a stagnating trend (Fig. 5.6a), the same was shown by Polyakov et al. (2023). A marked decrease in salinity (-0.015 $g\,kg^{-1}$ per annum) was observed in the last decade (Fig. 5.6b), starting around 2013. This trend is consistent across all sections and aligns with findings in the Fram Strait and Barents Sea (Kolås et al., 2023; Polyakov et al., 2023). The salinity maximum was found closer to the surface north of Svalbard during 2000-2009 (Fig. 5.9c), indicating shoaling of the AW and hence more sea ice melting during this decade. We observed a general warming of the shelf surface waters north of Svalbard (Sections C and D), replacing cold ASW or PW with warm ASW (Figs. 5.3 and 5.4), likely due to increased incoming solar radiation related to a reduced sea ice fraction in the area (Tab. 5.3 and Fig. 5.10).

The second research question we ask in Chapter 1 concerns the spatial characteristics of the SB along the continental shelf north of Svalbard from 1980 to 2020. We found the average July to November temperature and salinity gradients in the AW layer along the SB to be 0.16 °C/100km and -0.013 $g\,kg^{-1}$ /100km (Tab. 6.1), however, with significant differences between the different parts of the AW pathway in the SB. The temperature gradient corresponds to 250 $W\,m^{-2}$ to the upper ocean and 390 $W\,m^{-2}$ out of the ocean surface, which is less than Cokelet et al. (2008); Koläs & Fer (2018). We show that the AW barely lose or gain heat between Sections C and D (Fig. 5.9), and attribute this to a possible rejoining of the YB with the SB at 15 °E.

The third research question we ask in Chapter 1 concerns how atmospheric and oceanic factors influence the observed trends and variability north of Svalbard. The reduction in sea ice cover in 2010-2019 (Fig. 5.10) has enhanced air-ocean interactions north of Svalbard, leading to increased vertical heat fluxes (Tab. 5.5) and more deep convective mixing, as suggested by Athanase et al. (2020); Fu & Myers (2024). We see signs of this from the weakened surface stratification in Fig. 5.13 and the increased salinity of the surface water in 2010-2019 in all sections (Figs. 5.1 to 5.5 and 5.12). According to our analysis, the SB experienced significantly reduced heat loss

across all sections during the 2000-2009 period compared to other decades in our study (see Tab. 5.1). We attribute this reduced heat loss to the increased presence of melt water at the surface, resulting from anomalously warm and shallow AW during this decade (Fig. 5.9c). Additionally, warmer ambient water masses were observed both on the shelf and offshore, as depicted in Figs. 5.1 to 5.5 and 5.12. The insulating effect of the freshwater layer at the surface, combined with the reduced temperature gradient between the AW and adjacent water masses, diminished the heat loss from the AW as it propagated north of Svalbard.

To sum up, our study has highlighted hydrographic changes north of Svalbard over the past four decades, revealing significant spatial and temporal variability. The continuous temperature rise and shoaling of the AW core in the WSC, has brought increasingly warmer water to the north of Svalbard. This warming led to a dramatic decrease in sea ice, initially resulting in increased surface stratification that insulated the AW from the cold air. Additionally, changing wind patterns allowed AW to flow onto and replace the shelf water. Eventually, as the freshwater insulation diminished, the warm and shallow AW experienced increased heat loss to the atmosphere, causing deep convective mixing, which, in turn, led to a weakening or reversal of the temperature rise in the northern sections (C-E) and a salinification of the surface layer.

## 7.2   Future Work

The UNIS HD has proven to be a good tool to study decadal variability north of Svalbard. While past decades may suffer from insufficient data coverage, we now have the opportunity to support future studies by ensuring data coverage in the years to come. This will undoubtedly contribute to a deeper understanding of the temporal variability of the AW north of Svalbard. Therefore, we encourage more data collection in the future.

Moreover, calculating mean geostrophic velocities based on the density fields would enhance our understanding of the dynamics of the SB. Additionally, we would better be able to conserve the volume while computing heat loss in stream tubes between sections.

Furthermore, a more thorough investigation of the variability of the fronts separating the AW from adjacent water masses, both offshore and over the shelf, would deepen our knowledge of the lateral mixing between these water masses. This would provide a clearer picture of the temporal and spatial variability in the region north of Svalbard.
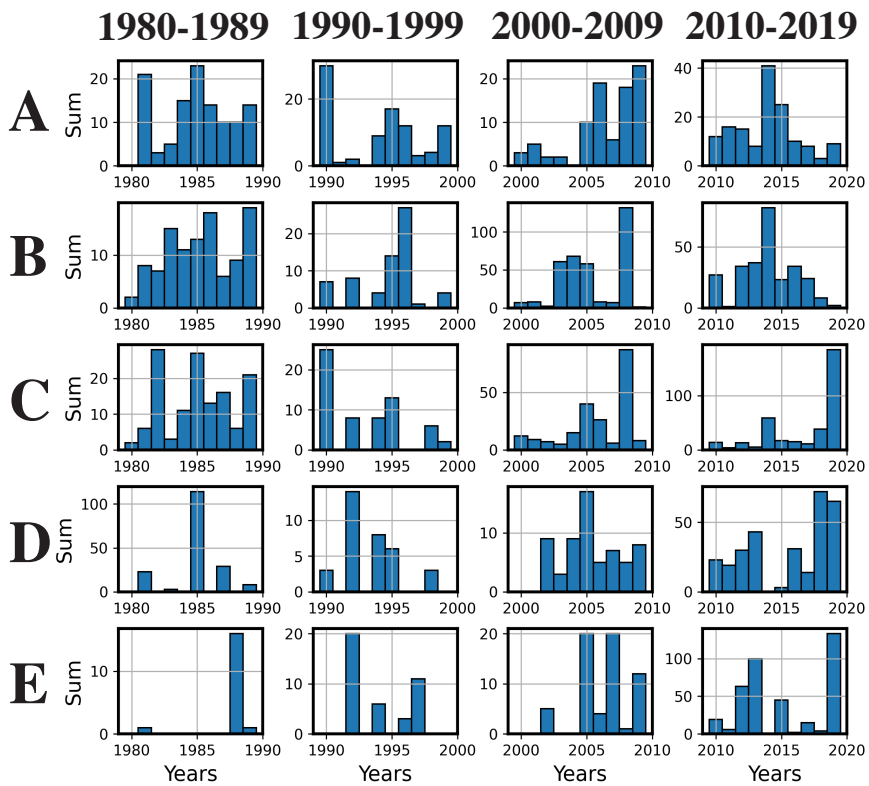
# Appendix A

# Data Quality



Figure A.1: Histograms showing the distribution of years included in the decadal mean for Sections A to E and the four decades (1980-1989, 1990-1999, 2000-2009 and 2010-2019).
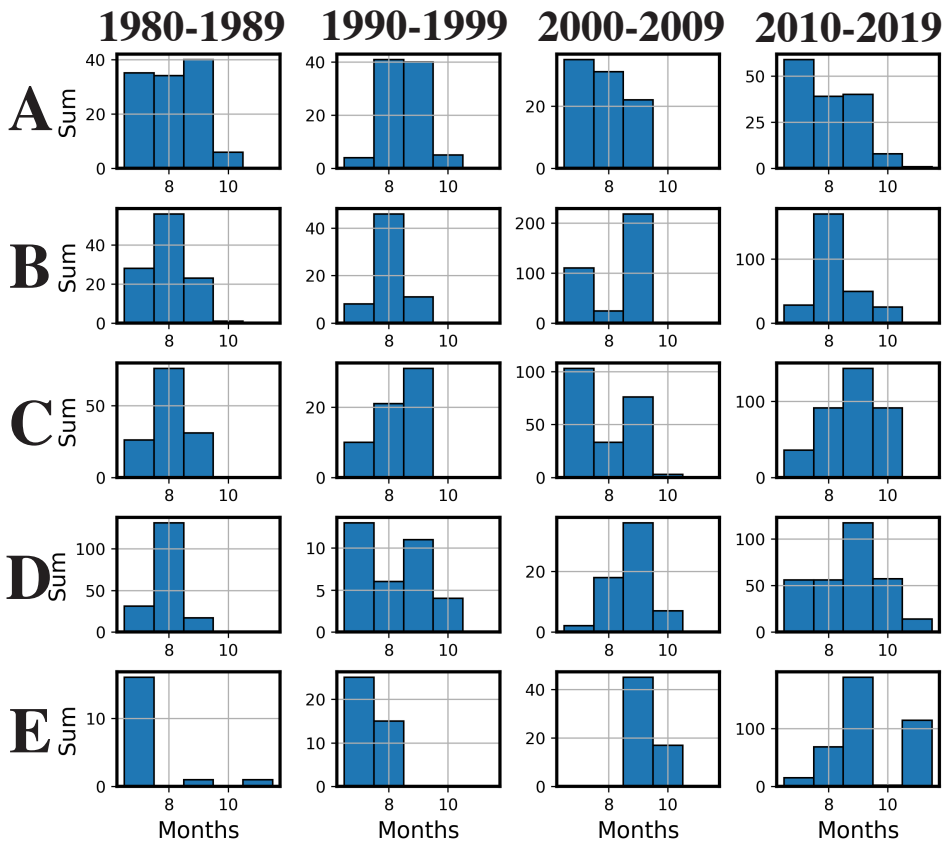
Figure A.2: Histograms showing the distribution of months included in the decadal mean for Sections A to E and the four decades (1980-1989, 1990-1999, 2000-2009 and 2010-2019).
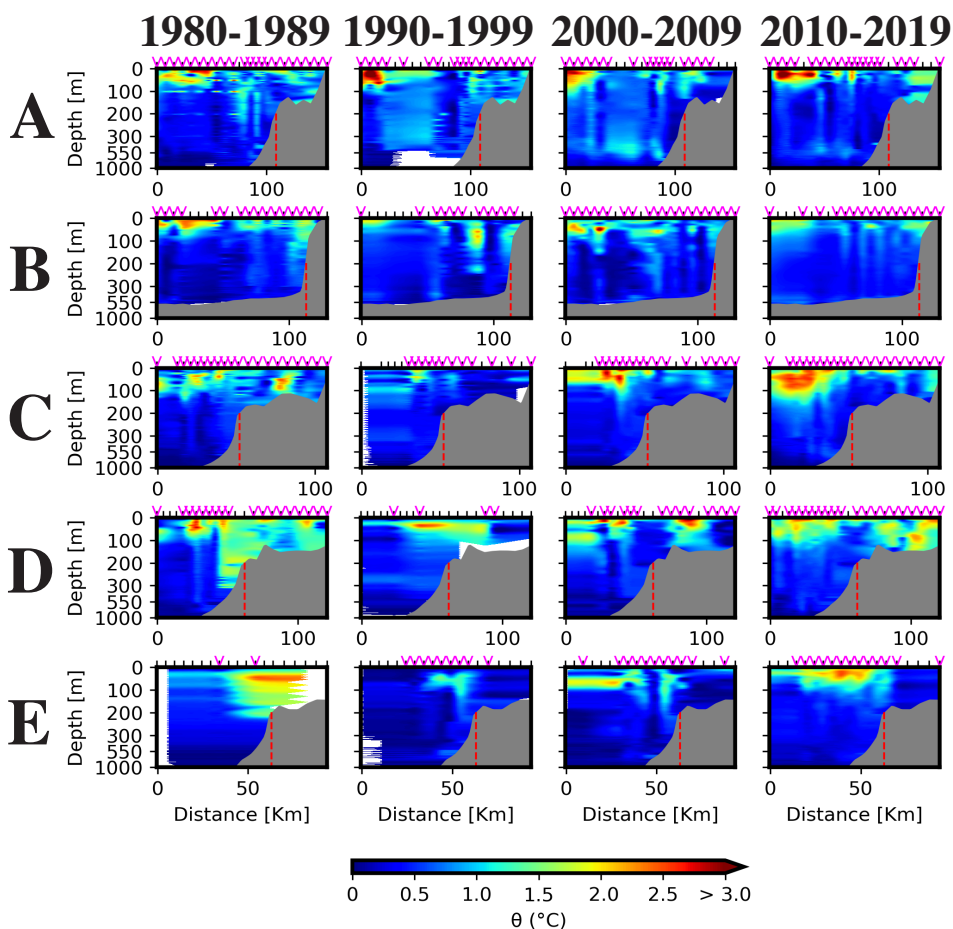
Figure A.3: Standard deviation of temperature for Sections A to E and the four decades (1980-1989, 1990-1999, 2000-2009 and 2010-2019). The bottom bathymetry (from Jakobsson et al., 2020) is delineated in grey, with the shelf break denoted by a dashed red line. The horizontal distance is relative to the offshore bin center, and magenta triangles indicate where we have observations. The vertical resolution is linear down to 300 m and transitioning to logarithmic thereafter.
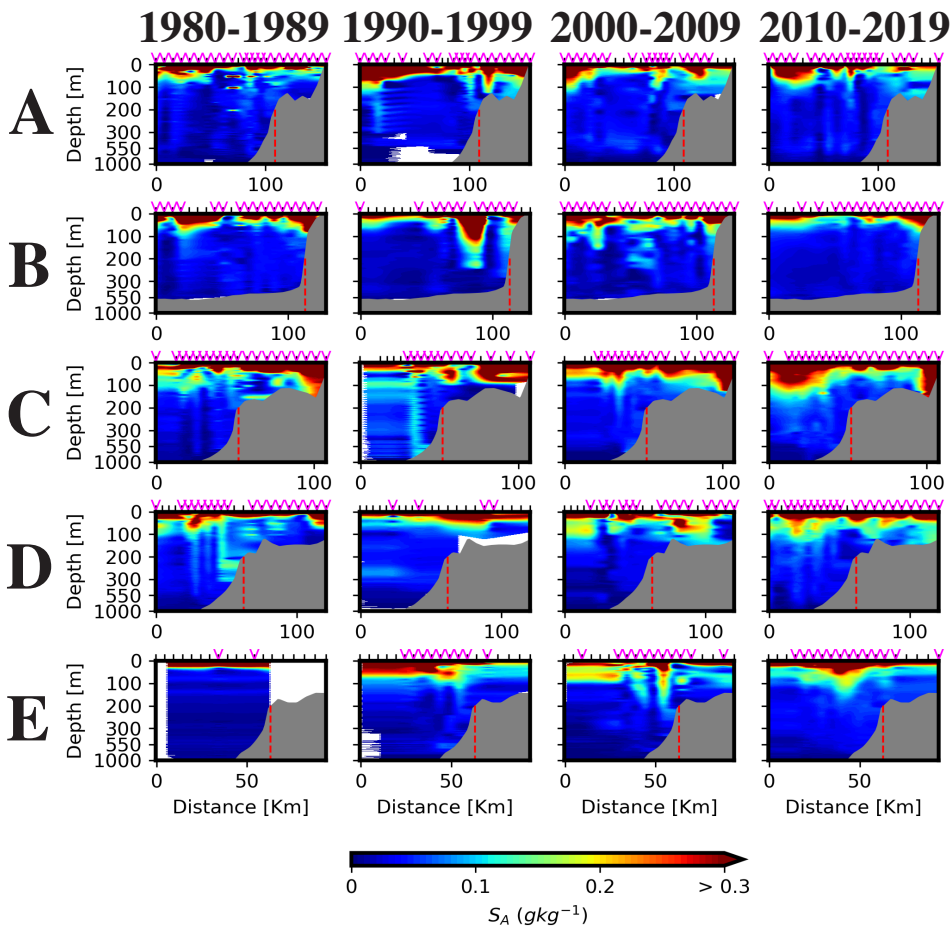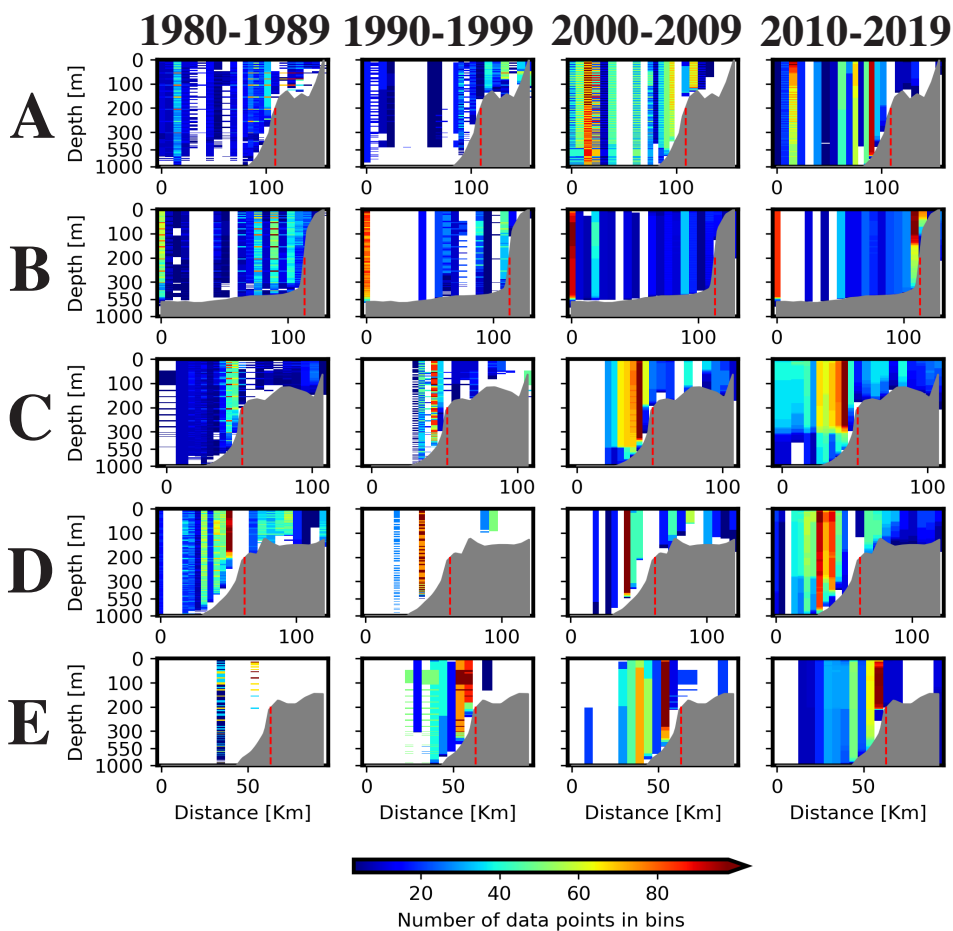
Figure A.4: Standard deviation of salinity for Sections A to E and the four decades (1980-1989, 1990-1999, 2000-2009 and 2010-2019). The bottom bathymetry (from Jakobsson et al., 2020) is delineated in grey, with the shelf break denoted by a dashed red line. The horizontal distance is relative to the offshore bin center, and magenta triangles indicate where we have observations. The vertical resolution is linear down to 300 m and transitioning to logarithmic thereafter.

Figure A.5: Number of data points contained in each bin for Sections A to E and the four decades (1980-1989, 1990-1999, 2000-2009 and 2010-2019). The bottom bathymetry (from Jakobsson et al., 2020) is delineated in grey, with the shelf break denoted by a dashed red line. The horizontal distance is relative to the offshore bin center, while the vertical resolution is linear down to 300 m and transitioning to logarithmic thereafter.
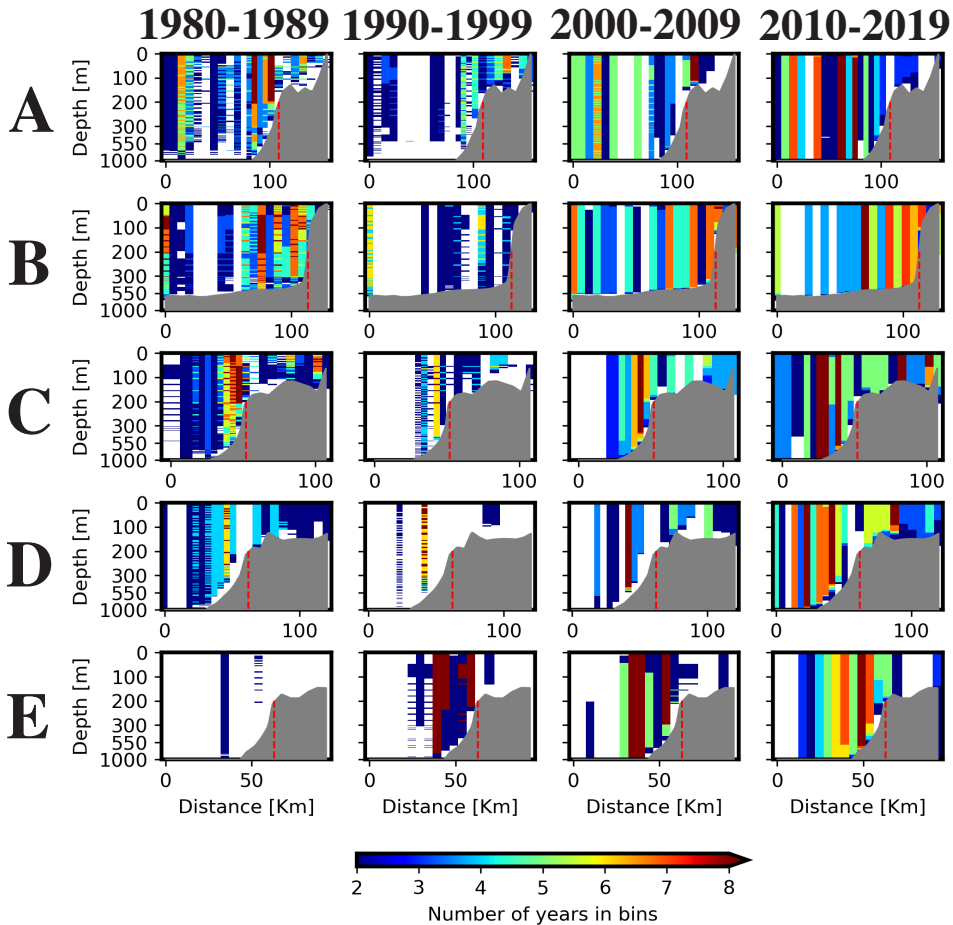
Figure A.6: Number of years contained in each bin for Sections A to E and the four decades (1980-1989, 1990-1999, 2000-2009 and 2010-2019). The bottom bathymetry (from Jakobsson et al., 2020) is delineated in grey, with the shelf break denoted by a dashed red line. The horizontal distance is relative to the offshore bin center, while the vertical resolution is linear down to 300 m and transitioning to logarithmic thereafter.
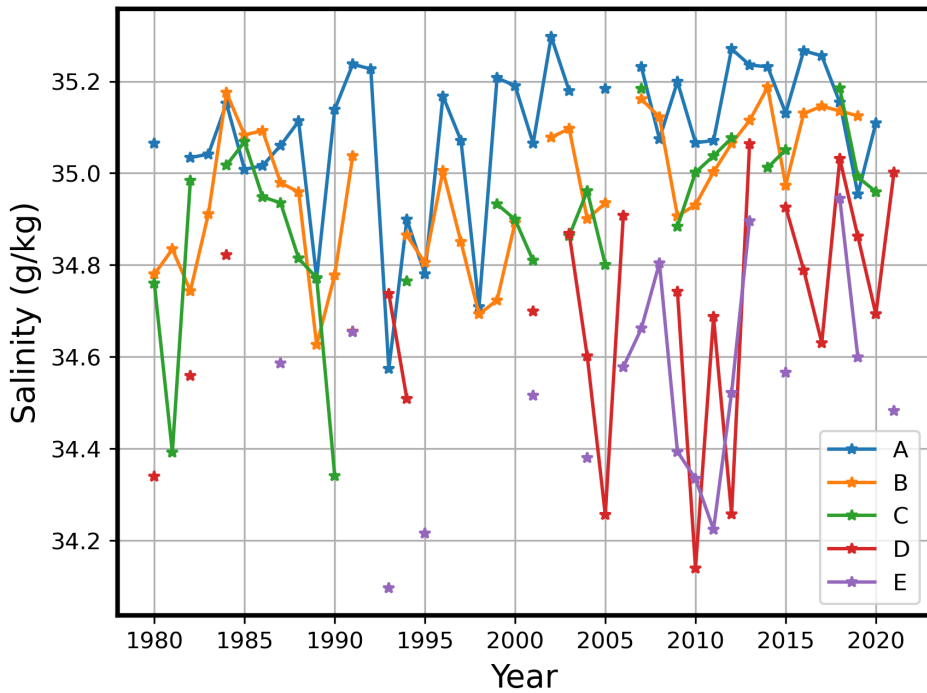
# Appendix B

# Water Properties



Figure B.1: Annual (1980-2021) mean July-to-November salinity from Sections A to E (surface layer; 0-100 m). Stars represent the values, while solid lines connect values of consecutive years

Table B.1: Temperature and salinity, and depths of the maximum values from Sections A to E and 1980 to 2020. Mean values are calculated from the AW-layer (100-500 m). Maximum values and their depths are found within the AW domain ($S_A > 35.06\,\mathrm{g\,kg^{-1}}$). Standard deviations are found from averaging the AW-layer in Figs. A.3 and A.4.

|   |   | 1980-1989 | 1990-1999 | 2000-2009 | 2010-2019 |
|---|---|---|---|---|---|
| A | $\Theta_{max}$ [°C] | 6.3 | 6.3 | 6.6 | 6.7 |
|   | $\overline{\Theta}$ [°C] | $2.8 \pm 0.5$ | $3.5 \pm 0.6$ | $3.5 \pm 0.5$ | $3.7 \pm 0.4$ |
|   | $P_{\Theta_{max}}$ [dbar] | 25 | 45 | 25 | 25 |
|   | $\overline{S_A}$ [g kg$^{-1}$] | $35.19 \pm 0.03$ | $35.14 \pm 0.03$ | $35.23 \pm 0.03$ | $35.25 \pm 0.04$ |
|   | $S_{A_{max}}$ [g kg$^{-1}$] | 35.25 | 35.24 | 35.31 | 35.30 |
|   | $P_{S_{max}}$ [dbar] | 85 | 100 | 85 | 100 |
| B | $\Theta_{max}$ [°C] | 5.0 | 5.8 | 6.6 | 6.8 |
|   | $\overline{\Theta}$ [°C] | $2.6 \pm 0.4$ | $3.2 \pm 0.4$ | $3.5 \pm 0.4$ | $3.7 \pm 0.5$ |
|   | $P_{\Theta_{max}}$ [dbar] | 35 | 45 | 35 | 0 |
|   | $\overline{S_A}$ [g kg$^{-1}$] | $35.18 \pm 0.03$ | $35.17 \pm 0.03$ | $35.21 \pm 0.03$ | $35.25 \pm 0.03$ |
|   | $S_{A_{max}}$ [g kg$^{-1}$] | 35.24 | 35.24 | 35.31 | 35.30 |
|   | $P_{S_{max}}$ [dbar] | 95 | 100 | 100 | 100 |
| C | $\Theta_{max}$ [°C] | 4.4 | 5.7 | 5.6 | 5.3 |
|   | $\overline{\Theta}$ [°C] | $2.0 \pm 0.4$ | $2.9 \pm 0.4$ | $3.0 \pm 0.4$ | $3.0 \pm 0.5$ |
|   | $P_{\Theta_{max}}$ [dbar] | 40 | 50 | 55 | 55 |
|   | $\overline{S_A}$ [g kg$^{-1}$] | $35.14 \pm 0.04$ | $35.13 \pm 0.05$ | $35.19 \pm 0.05$ | $35.17 \pm 0.05$ |
|   | $S_{A_{max}}$ [g kg$^{-1}$] | 35.23 | 35.20 | 35.25 | 35.26 |
|   | $P_{S_{max}}$ [dbar] | 105 | 150 | 75 | 110 |
| D | $\Theta_{max}$ [°C] | 4.2 | 4.1 | 4.8 | 5.0 |
|   | $\overline{\Theta}$ [°C] | $2.2 \pm 0.7$ | $2.8 \pm 0.5$ | $3.1 \pm 0.4$ | $2.9 \pm 0.5$ |
|   | $P_{\Theta_{max}}$ [dbar] | 50 | 80 | 80 | 45 |
|   | $\overline{S_A}$ [g kg$^{-1}$] | $35.12 \pm 0.06$ | $35.17 \pm 0.04$ | $35.17 \pm 0.03$ | $35.15 \pm 0.05$ |
|   | $S_{A_{max}}$ [g kg$^{-1}$] | 35.19 | 35.19 | 35.24 | 35.24 |
|   | $P_{S_{max}}$ [dbar] | 265 | 200 | 165 | 210 |
| E | $\Theta_{max}$ [°C] | 1.8 | 2.9 | 4.7 | 3.7 |
|   | $\overline{\Theta}$ [°C] | $1.6 \pm 0.5$ | $2.3 \pm 0.3$ | $2.9 \pm 0.3$ | $2.5 \pm 0.4$ |
|   | $P_{\Theta_{max}}$ [dbar] | 205 | 115 | 85 | 110 |
|   | $\overline{S_A}$ [g kg$^{-1}$] | $35.11 \pm 0.01$ | $35.11 \pm 0.03$ | $35.15 \pm 0.03$ | $35.13\,0.04$ |
|   | $S_{A_{max}}$ [g kg$^{-1}$] | 35.14 | 35.17 | 35.25 | 35.21 |
|   | $P_{S_{max}}$ [dbar] | 365 | 310 | 125 | 250 |

# Bibliography

Aagaard, K., Foldvik, A., & Hillman, S. R. (1987). The West Spitsbergen Current: Disposition and water mass transformation. *Journal of Geophysical Research: Oceans*, *92*, 3778–3784. doi:10.1029/JC092iC04p03778.

Aagaard, K., Swift, J. H., & Carmack, E. C. (1985). Thermohaline circulation in the Arctic Mediterranean Seas. *Journal of Geophysical Research: Oceans*, *90*, 4833–4846. doi:10.1029/jc090ic03p04833.

Artana, C., Provost, C., Koenig, Z., Athanase, M., & Asgari, A. (2022). Atlantic Water Inflow Through the Yermak Pass Branch: Evolution Since 2007. *Journal of Geophysical Research: Oceans*, *127*. doi:10.1029/2021JC018006.

Årthun, M., Eldevik, T., Smedsrud, L. H., Skagseth, & Ingvaldsen, R. B. (2012). Quantifying the influence of atlantic heat on barents sea ice variability and retreat. *Journal of Climate*, *25*, 4736–4743. doi:10.1175/JCLI-D-11-00466.1.

Athanase, M., Provost, C., Pérez-Hernández, M. D., Sennéchael, N., Bertosio, C., Artana, C., Garric, G., & Lellouche, J. M. (2020). Atlantic Water Modification North of Svalbard in the Mercator Physical System From 2007 to 2020. *Journal of Geophysical Research: Oceans*, *125*. doi:10.1029/2020JC016463.

Barton, B. I., Lenn, Y. D., & Lique, C. (2018). Observed atlantification of the Barents Sea causes the Polar Front to limit the expansion of winter sea ice. *Journal of Physical Oceanography*, *48*, 1849–1866. doi:10.1175/JPO-D-18-0003.1.

Beszczynska-Möller, A. B.-M., Fahrbach, E., Schauer, U., & Hansen, E. (2012). Variability in Atlantic water temperature and transport at the entrance to the Arctic Ocean, 19972010. *ICES Journal of Marine Science*, *69*, 852–863. doi:10.1093/icesjms/fss056.

Bourke, R. H., Weigel, A. M., & Paquette, R. G. (1988). The westward turning branch of the West Spitsbergen Current. *Journal of Geophysical Research: Oceans*, *93*, 14065–14077. doi:10.1029/jc093ic11p14065.

Boyd, T. J., & D'Asaro, E. A. (1994). Cooling of the West Spitsbergen Current: wintertime observations west of Svalbard. *Journal of Geophysical Research*, *99*. doi:10.1029/94jc01824.

Carmack, E., Polyakov, I., Padman, L., Fer, I., Hunke, E., Hutchings, J., Jackson, J., Kelley, D., Kwok, R., Layton, C., Melling, H., Perovich, D., Persson, O., Ruddick, B., Timmermans, M. L., Toole, J., Ross, T., Vavrus, S., & Winsor, P. (2015). Toward quantifying the increasing role of oceanic heat in sea ice loss in the new arctic. *Bulletin of the American Meteorological Society*, *96*, 2079–2105. doi:10.1175/BAMS-D-13-00177.1.

Cokelet, E. D., Tervalon, N., & Bellingham, J. G. (2008). Hydrography of the West Spitsbergen Current, Svalbard Branch: Autumn 2001. *Journal of Geophysical Research: Oceans*, *113*. doi:10.1029/2007JC004150.

Cottier, F. R., Nilsen, F., Enall, M. E., Gerland, S., Tverberg, V., & Svendsen, H. (2007). Wintertime warming of an Arctic shelf in response to large-scale atmospheric circulation. *Geophysical Research Letters*, *34*. doi:10.1029/2007GL029948.

Crews, L., Sundfjord, A., Albretsen, J., & Hattermann, T. (2018). Mesoscale Eddy Activity and Transport in the Atlantic Water Inflow Region North of Svalbard. *Journal of Geophysical Research: Oceans*, *123*, 201–215. doi:10.1002/2017JC013198.

Fer, I., Peterson, A. K., & Nilsen, F. (2023). Atlantic Water Boundary Current Along the Southern Yermak Plateau, Arctic Ocean. *Journal of Geophysical Research: Oceans*, *128*. doi:10.1029/2023jc019645.

Fransson, A. (2022). CTD data from Nansen Legacy Cruise - Arctic Basin Joint Cruise 2-2, . doi:https://doi.org/10.21335/NMDC-1814168447.

Fu, C., & Myers, P. G. (2024). Exceptional sea ice loss leading to anomalously deep winter convection north of Svalbard in 2018. *Climate Dynamics*, *62*, 2349–2367. doi:10.1007/s00382-023-07027-8.

Gascard, J.-C., Richez, C., & Rouault, C. (1995). New insights on large-scale oceanography in Fram Strait: The West Spitsbergen Current. In *W.O. Smith, Jr., & J. M. Greibmeier (Eds.) Arctic oceanography, marginal ice zones and continental shelves* (pp. 131–182). Washington D.C.: American Geophysical Union volume 49.

Good, S., Fiedler, E., Mao, C., Martin, M. J., Maycock, A., Reid, R., Roberts-Jones, J., Searle, T., Waters, J., While, J., & Worsfold, M. (2020). The current configuration of the OSTIA system for operational production of foundation sea surface temperature and ice concentration analyses. *Remote Sensing*, *12*. doi:10.3390/rs12040720.

Hattermann, T., Isachsen, P. E., Von Appen, W. J., Albretsen, J., & Sundfjord, A. (2016). Eddy-driven recirculation of Atlantic Water in Fram Strait. *Geophysical Research Letters*, *43*, 3406–3414. doi:10.1002/2016GL068323.

Helland-Hansen, B., & Nansen, F. (1909). The Norwegian Sea. Its physical oceanography based upon the Norwegian Researches 1900-1904. In *Report on Norwegian Fishery and Marine Investigations* (pp. 1–359).

Helland-Hansen, B., & Nansen, F. (1912). The sea west ofSpitsbergen, the oceanographic observations of the Isachsen Spitsbergen Expedition in 1910. *Videnskapsselskapets. Skrifter I. Matematisk-Naturvidenskabelig Klasse*, *12*, 1–89.

Hersbach, H., Bell, B., Berrisford, P., Biavati, G., Horányi, A., Muñoz Sabater, J., & Nicolas, J. (2023). ERA5 hourly data on single levels from 1940 to present. *Copernicus Climate Change Service (C3S) Climate Data Store (CDS)*, . doi:10.24381/cds.adbb2d47.

Hofmann, Z., von Appen, W. J., & Wekerle, C. (2021). Seasonal and Mesoscale Variability of the Two Atlantic Water Recirculation Pathways in Fram Strait. *Journal of Geophysical Research: Oceans*, *126*. doi:10.1029/2020JC017057.

IPCC (2022). Technical Summary. In I. P. o. C. C. (IPCC) (Ed.), *The Ocean and Cryosphere in a Changing Climate: Special Report of the Intergovernmental Panel on Climate Change* (pp. 39–70). Cambridge: Cambridge University Press. URL: https://www.cambridge.org/core/product/3428BF3C6ADE0C52755DBC3AA5CFE48B. doi:DOI:10.1017/9781009157964.002.

Jakobsson, M., Mayer, L. A., Bringensparr, C., Castro, C. F., Mohammad, R., Johnson, P., Ketter, T., Accettella, D., Amblas, D., An, L., Arndt, J. E., Canals, M., Casamor, J. L., Chauché, N., Coakley, B., Danielson, S., Demarte, M., Dickson, M. L., Dorschel, B., Dowdeswell, J. A., Dreutter, S., Fremand, A. C., Gallant, D., Hall, J. K., Hehemann, L., Hodnesdal, H., Hong, J., Ivaldi, R., Kane, E., Klaucke, I., Krawczyk, D. W., Kristoffersen, Y., Kuipers, B. R., Millan, R., Masetti, G., Morlighem, M., Noormets, R., Prescott, M. M., Rebesco, M., Rignot, E., Semiletov, I., Tate, A. J., Travaglini, P., Velicogna, I., Weatherall, P., Weinrebe, W., Willis, J. K., Wood, M., Zarayskaya, Y., Zhang, T., Zimmermann, M., & Zinglersen, K. B. (2020). The International Bathymetric Chart of the Arctic Ocean Version 4.0. *Scientific Data*, *7*. doi:10.1038/s41597-020-0520-9.

Jones, E. (2022). CTD data from Nansen Legacy Cruise - Joint cruise 2-1, . doi:https://doi.org/10.21335/NMDC-2085836005.

Koenig, Z., Kalhagen, K., Kolås, E., Fer, I., Nilsen, F., & Cottier, F. (2022). Atlantic Water Properties, Transport and Heat Loss From Mooring Observations North of Svalbard. *Journal of Geophysical Research: Oceans*, *127*. doi:10.1029/2022jc018568.

Koenig, Z., Provost, C., Sennéchael, N., Garric, G., & Gascard, J. C. (2017a). The Yermak Pass Branch: A Major Pathway for the Atlantic Water North of Svalbard? *Journal of Geophysical Research: Oceans*, *122*, 9332–9349. doi:10.1002/2017JC013271.

Koenig, Z., Provost, C., Villacieros-Robineau, N., Sennéchael, N., Meyer, A., Lellouche, J. M., & Garric, G. (2017b). Atlantic waters inflow north of Svalbard: Insights from IAOOS observations and Mercator Ocean global operational system during N-ICE2015. *Journal of Geophysical Research: Oceans*, *122*, 1254–1273. doi:10.1002/2016JC012424.

Koläs, E., & Fer, I. (2018). Hydrography, transport and mixing of the West Spitsbergen Current: The Svalbard Branch in summer 2015. *Ocean Science*, *14*, 1603–1618. doi:10.5194/OS-14-1603-2018.

Kolås, E. H., Baumann, T. M., Skogseth, R., Koenig, Z., & Fer, I. (2023). *Western Barents Sea Circulation and Hydrography, past and present*. Technical Report. doi:10.22541/essoar.169203078.81082540/v1.

Lind, S., Ingvaldsen, R. B., & Furevik, T. (2018). Arctic warming hotspot in the northern Barents Sea linked to declining sea-ice import. *Nature Climate Change*, *8*, 634–639. doi:10.1038/s41558-018-0205-y.

McDougall, T. J., & Barker, P. M. (2011). *Getting started with TEOS-10 and the Gibbs Seawater (GSW) Oceanographic Toolbox*. SCOR/IAPSO WG127.

Merchel, M., & Walczowski, W. (2020). Increases in the temperature and salinity of deep and intermediate waters in the West Spitsbergen Current region in 1997–2016. *Oceanologia*, *62*, 501–510. doi:10.1016/j.oceano.2020.08.001.

Moore, G. W., Våge, K., Renfrew, I. A., & Pickart, R. S. (2022). Sea-ice retreat suggests re-organization of water mass transformation in the Nordic and Barents Seas. *Nature Communications*, *13*. doi:10.1038/s41467-021-27641-6.

Muckenhuber, S., Nilsen, F., Korosov, A., & Sandven, S. (2016). Sea ice cover in Isfjorden and Hornsund, Svalbard (2000-2014) from remote sensing data. *Cryosphere*, *10*, 149–158. doi:10.5194/tc-10-149-2016.

Muilwijk, M., Smedsrud, L. H., Ilicak, M., & Drange, H. (2018). Atlantic Water Heat Transport Variability in the 20th Century Arctic Ocean From a Global Ocean Model and Observations. *Journal of Geophysical Research: Oceans*, *123*, 8159–8179. doi:10.1029/2018JC014327.

Nansen, F. (1902). *Oceanography of the North Polar Basin, in Norwegian North Polar Expedition 1893-96* volume 3.

Nilsen, F., Ersdal, E. A., & Skogseth, R. (2021). Wind-Driven Variability in the Spitsbergen Polar Current and the Svalbard Branch Across the Yermak

Plateau. *Journal of Geophysical Research: Oceans*, *126*. doi:10.1029/2020JC016734.

Nilsen, F., Skogseth, R., Vaardal-Lunde, J., & Inall, M. (2016). A simple shelf circulation model: Intrusion of Atlantic water on the West Spitsbergen Shelf. *Journal of Physical Oceanography*, *46*, 1209–1230. doi:10.1175/JPO-D-15-0058.1.

Onarheim, I. H., Eldevik, T., Smedsrud, L. H., & Stroeve, J. C. (2018). Seasonal and regional manifestation of Arctic sea ice loss. *Journal of Climate*, *31*, 4917–4932. doi:10.1175/JCLI-D-17-0427.1.

Onarheim, I. H., Smedsrud, L. H., Ingvaldsen, R. B., & Nilsen, F. (2014). Loss of sea ice during winter north of Svalbard. *Tellus, Series A: Dynamic Meteorology and Oceanography*, *66*. doi:10.3402/tellusa.v66.23933.

Orvik, K. A., & Niiler, P. (2002). Major pathways of Atlantic water in the northern North Atlantic and Nordic Seas toward Arctic. *Geophysical Research Letters*, *29*. doi:10.1029/2002GL015002.

Oziel, L., Baudena, A., Ardyna, M., Massicotte, P., Randelhoff, A., Sallée, J. B., Ingvaldsen, R. B., Devred, E., & Babin, M. (2020). Faster Atlantic currents drive poleward expansion of temperate phytoplankton in the Arctic Ocean. *Nature Communications*, *11*. doi:10.1038/s41467-020-15485-5.

Parkinson, C. L., & Cavalieri, D. J. (2008). Arctic sea ice variability and trends, 1979-2006. *Journal of Geophysical Research: Oceans*, *113*. doi:10.1029/2007JC004558.

Pavlov, A. K., Tverberg, V., Ivanov, B. V., Nilsen, F., Falk-Petersen, S., & Granskog, M. A. (2013). Warming of Atlantic water in two west Spitsbergen fjords over the last century (1912-2009). doi:10.3402/polar.v32i0.11206.

Pérez-Hernández, M. D., Pickart, R. S., Torres, D. J., Bahr, F., Sundfjord, A., Ingvaldsen, R., Renner, A. H., Beszczynska-Möller, A., von Appen, W. J., & Pavlov, V. (2019). Structure, Transport, and Seasonality of the Atlantic Water Boundary Current North of Svalbard: Results From a

Yearlong Mooring Array. *Journal of Geophysical Research: Oceans*, *124*, 1679–1698. doi:10.1029/2018JC014759.

Perkin, R. G., & Lewis, E. L. (1984). Mixing in the West Spitsbergen Current. *Journal of Physical Oceanography*, *14*, 1315–1325. doi:https://doi.org/10.1175/1520-0485(1984)014<1315:MITWSC>2.0.CO;2.

Polyakov, I. V., Alkire, M. B., Bluhm, B. A., Brown, K. A., Carmack, E. C., Chierici, M., Danielson, S. L., Ellingsen, I., Ershova, E. A., Gårdfeldt, K., Ingvaldsen, R. B., Pnyushkov, A. V., Slagstad, D., & Wassmann, P. (2020). Borealization of the Arctic Ocean in Response to Anomalous Advection From Sub-Arctic Seas. *Frontiers in Marine Science*, *7*. doi:10.3389/fmars.2020.00491.

Polyakov, I. V., Ingvaldsen, R. B., Pnyushkov, A. V., Bhatt, U. S., Francis, J. A., Janout, M., Kwok, R., & Skagseth, (2023). *Fluctuating Atlantic inflows modulate Arctic atlantification*. Technical Report. doi:10.1126/science.adh5158.

Polyakov, I. V., Pnyushkov, A. V., Alkire, M. B., Ashik, I. M., Baumann, T. M., Carmack, E. C., Goszczko, I., Guthrie, J., Ivanov, V. V., Kanzow, T., Krishfield, R., Kwok, R., Sundfjord, A., Morison, J., Rember, R., & Yulin, A. (2017). Greater role for Atlantic inflows on sea-ice loss in the Eurasian Basin of the Arctic Ocean. *Science*, (pp. 285–291). doi:10.1126/science.aai8204.

Reigstad, M. (2022). CTD data from Nansen Legacy Cruise - Seasonal cruise Q3, . doi:https://doi.org/10.21335/NMDC-1107597377.

Saloranta, T. M., & Haugan, P. M. (2001). Interannual variability in the hydrography of Atlantic water northwest of Svalbard. *Journal of Geophysical Research: Oceans*, *106*, 13931–13943. doi:10.1029/2000JC000478.

Saloranta, T. M., & Haugan, P. M. (2004). *Northward cooling and freshening of the West Spitsbergen Current*. Technical Report. doi:https://doi.org/10.3402/polar.v23i1.6268.

Schauer, U., Fahrbach, E., Osterhus, S., & Rohardt, G. (2004). Arctic warming through the Fram Strait: Oceanic heat transport from 3 years of

measurements. *Journal of Geophysical Research: Oceans*, *109*. doi:10.1029/2003JC001823.

Schauer, U., Loeng, H., Rudels, B., Ozhigin, V. K., & Dieck, W. (2002). *Atlantic Water flow through the Barents and Kara Seas*. Technical Report. doi:https://doi.org/10.1016/S0967-0637(02)00125-5.

Skogseth, R., Ellingsen, P., Berge, J., Cottier, F., Falk-Petersen, S., Ivanov, B., Nilsen, F., Søreide, J., & Vader, A. (2019). UNIS hydrographic database [Data set]. *Norwegian Polar Institutes*, . doi:https://doi.org/10.21334/unis-hydrography.

Skogseth, R., Olivier, L. L., Nilsen, F., Falck, E., Fraser, N., Tverberg, V., Ledang, A. B., Vader, A., Jonassen, M. O., Søreide, J., Cottier, F., Berge, J., Ivanov, B. V., & Falk-Petersen, S. (2020). Variability and decadal trends in the Isfjorden (Svalbard) ocean climate and circulation – An indicator for climate change in the European Arctic. *Progress in Oceanography*, *187*. doi:10.1016/j.pocean.2020.102394.

Smedsrud, L. H., Esau, I., Ingvaldsen, R. B., Eldevik, T., Haugan, P. M., Li, C., Lien, V. S., Olsen, A., Omar, A. M., Risebrobakken, B., Sandø, A. B., Semenov, V. A., & Sorokina, S. A. (2013). The role of the Barents Sea in the Arctic climate system. *Reviews of Geophysics*, *51*, 415–449. doi:10.1002/rog.20017.

Smith, W. H. F., & Wessel, P. (1990). *Gri-ding with continuous curvature splines in tension*. Technical Report 3. doi:10.1190/1.1442837.

Søreide, J. (2022). CTD data from Nansen Legacy Cruise - Seasonal cruise Q4, . doi:https://doi.org/10.21335/NMDC-301551919.

Steele, M., & Ermold, W. (2015). Loitering of the retreating sea ice edge in the Arctic Seas. *Journal of Geophysical Research: Oceans*, *120*, 7699–7721. doi:10.1002/2015JC011182.

Stroeve, J. C., Serreze, M. C., Holland, M. M., Kay, J. E., Malanik, J., & Barrett, A. P. (2012). The Arctic's rapidly shrinking sea ice cover: A research synthesis. *Climatic Change*, *110*, 1005–1027. doi:10.1007/s10584-011-0101-1.

Sundfjord, A. (2022). CTD data from Nansen Legacy Cruise - Mooring service cruise 2019, . doi:https://doi.org/10.21335/NMDC-2135074338.

Swift, J. H., & Aagaard, K. (1981). *Seasonal transitions and water mass formation in the Iceland and Greenland seas\**. Technical Report 10. doi:https://doi.org/10.1016/0198-0149(81)90050-9.

Teigen, S. H., Nilsen, F., & Gjevik, B. (2010). Barotropic instability in the West Spitsbergen Current. *Journal of Geophysical Research: Oceans*, *115*. doi:10.1029/2009JC005996.

Teigen, S. H., Nilsen, F., Skogseth, R., Gjevik, B., & Beszczynska-Möller, A. (2011). Baroclinic instability in the West Spitsbergen Current. *Journal of Geophysical Research: Oceans*, *116*. doi:10.1029/2011JC006974.

Torres-Valdés, S., Tsubouchi, T., Bacon, S., Naveira-Garabato, A. C., Sanders, R., McLaughlin, F. A., Petrie, B., Kattner, G., Azetsu-Scott, K., & Whitledge, T. E. (2013). Export of nutrients from the Arctic Ocean. *Journal of Geophysical Research: Oceans*, *118*, 1625–1644. doi:10.1002/jgrc.20063.

Tverberg, V., Skogseth, R., Cottier, F., Sundfjord, A., Walczowski, W., Inall, M. E., Falck, E., Pavlova, O., & Nilsen, F. (2019). The Kongsfjorden Transect: Seasonal and Inter-annual Variability in Hydrography. (pp. 49–104). doi:10.1007/978-3-319-46425-1{\_}3.

Våge, K., Pickart, R. S., Pavlov, V., Lin, P., Torres, D. J., Ingvaldsen, R., Sundfjord, A., & Proshutinsky, A. (2016). The Atlantic Water boundary current in the Nansen Basin: Transport and mechanisms of lateral exchange. *Journal of Geophysical Research: Oceans*, *121*, 6946–6960. doi:10.1002/2016JC011715.

Virtanen, P., Gommers, R., Oliphant, T. E., Haberland, M., Reddy, T., Cournapeau, D., Burovski, E., Peterson, P., Weckesser, W., Bright, J., van der Walt, S. J., Brett, M., Wilson, J., Millman, K. J., Mayorov, N., Nelson, A. R. J., Jones, E., Kern, R., Larson, E., Carey, C. J., Polat, I., Feng, Y., Moore, E. W., VanderPlas, J., Laxalde, D., Perktold, J., Cimrman, R., Henriksen, I., Quintero, E. A., Harris, C. R., Archibald, A. M.,

Ribeiro, A. H., Pedregosa, F., van Mulbregt, P., & SciPy 1.0 Contributors (2020).